

Effective Dark Matter Model: Relic density, CDMS II, Fermi LAT and LHC

Hao Zhang,^{1,2,*} Qing-Hong Cao,^{1,2,3,†} Chuan-Ren Chen,^{4,‡} and Chong Sheng Li^{1,§}

¹*Department of Physics and State Key Laboratory of Nuclear Physics and Technology,*

Peking University, Beijing 100871, China

²*Enrico Fermi Institute, University of Chicago, Chicago, Illinois 60637, U.S.A.*

³*HEP Division, Argonne National Laboratory, Argonne, Illinois 60439, U.S.A.*

⁴*Institute for the Physics and Mathematics of the Universe,*

The University of Tokyo, Chiba 277 8568, Japan

Abstract

The Cryogenic Dark Matter Search recently announced the observation of two signal events with a 77% confidence level. Although statistically inconclusive, it is nevertheless suggestive. In this work we present a model-independent analysis on the implication of direct and indirect searches for the dark matter using effective operator approach. Assuming that the interactions between (scalar, fermion or vector) dark matter and the standard model are mediated by unknown new physics at the scale Λ , we examine various dimension-6 tree-level induced operators and constrain them using the current experimental data, including the WMAP data of the relic abundance, CDMS II direct detection of the spin-independent scattering, and indirect detection data (Fermi LAT cosmic gamma-ray). Finally, the LHC search is also explored.

*Electronic address: haozhang.pku@pku.edu.cn

†Electronic address: caoq@hep.anl.gov

‡Electronic address: chuan-ren.chen@ipmu.jp

§Electronic address: csl@pku.edu.cn

Contents	
I. Introduction	4
II. General aspects of cold dark matter	6
III. Fermionic dark matter χ	9
A. Relic abundance	11
B. Direct detection of χ	13
C. Indirect gamma-ray detection of χ	16
D. Collider search for χ	18
IV. Scalar DM φ	23
A. Relic abundance	26
B. Direct Search	28
C. Indirect search	30
D. Collider search	32
V. Vector dark matter \mathcal{Z}	33
A. Relic abundance	34
B. Direct Detection	35
C. Indirect search	36
D. Collider search	38
VI. Conclusion	38
Acknowledgments	42
A. Relic abundance	43
B. Dark matter annihilation	44
1. Fermionic dark matter annihilation	44
a. $\chi\bar{\chi} \rightarrow f\bar{f}$	45
b. $\chi\bar{\chi} \rightarrow Z \rightarrow f\bar{f}$	45
c. $\chi\bar{\chi} \rightarrow hZ$	46
d. $\chi\bar{\chi} \rightarrow Z \rightarrow hZ$	46

e. $\chi\bar{\chi} \rightarrow Z \rightarrow W^+W^-$	47
2. Scalar dark matter annihilation	47
a. $\varphi\varphi \rightarrow f\bar{f}$	47
b. $\varphi\varphi \rightarrow WW/ZZ$	48
c. $\varphi\varphi \rightarrow hh$	49
3. Vector dark matter annihilation	49
a. $ZZ \rightarrow hh$	49
b. $ZZ \rightarrow h \rightarrow hh$	50
c. $ZZ \rightarrow h \rightarrow f\bar{f}$	50
d. $ZZ \rightarrow h \rightarrow WW/ZZ$	50
C. Dark matter direct detection	51
1. Fermionic DM-nucleon interaction	51
2. Scalar DM-nucleon interaction	53
3. Vector DM-nucleon interaction	54
D. Dark matter indirect detection from gamma-ray	55
References	57

I. INTRODUCTION

The observational data that have accumulated for decades point to the existence of a significant amount of dark matter (DM), and the nature of this substance has become one of the key problems at the interface between particle physics, astrophysics and cosmology. Since the Standard Model (SM) of particle physics does not possess any candidate for such dark matter, this problem constitutes a major indication for new physics beyond the SM. Our current knowledge of the proprieties of DM are inferred solely from astrophysical and cosmological observations, which provide no information about its most basic characteristics such as the spin and mass. Recently, many anomalies in various cosmic-ray observations, for example, INTEGRAL [1], ATIC [2], PAMELA [3] and Fermi LAT [4], were found and attracted many investigators' attention. Due to our poor understanding of astrophysical backgrounds, it is not affirmative to say those excesses are indeed caused by dark matter. On the other hand, the direct detection is considered more robust. The Cryogenic Dark Matter Search (CDMS II) recently announced the observation of two signal events with a 77% confidence level [5] and additional two events just outside the signal region. While statistically such an observation is not significant, it is nevertheless suggestive and stimulates a lot of studies of its implication [6–15].

There are many proposals for the dark matter in the literature: the lightest supersymmetric particle in the supersymmetric models with conserved R -parity [16, 17], the lightest KK excitation in the universal extra dimension models with conserved KK-parity [18–20], the lightest T-odd particle in the little Higgs models with conserved T-parity [21–23], and dark scalar models [24–35], etc. Beside the DM candidate, all the new physics models mentioned above also provide many novel predictions that can (and will) be probed at the Large Hadron Collider (LHC); observing any such new effect will shed light on the theory underlying the SM. But it is also possible that all new physics effects will be hidden from direct observation at the LHC [36]. This is the case, for example, when the DM belongs to a “hidden sector” that interacts very weakly with the SM particles (e.g. if the mediating particles are very heavy), see Fig. 1 for illustration. Communication between the hidden sector and the SM can then be described by an effective field theory (EFT). In this paper, we investigate the dimension six, tree-level generated and $SU(3)_c \times SU(2)_L \times U(1)_Y$ invariant effective operators, which describe the interactions of DM and SM particles. Similar studies

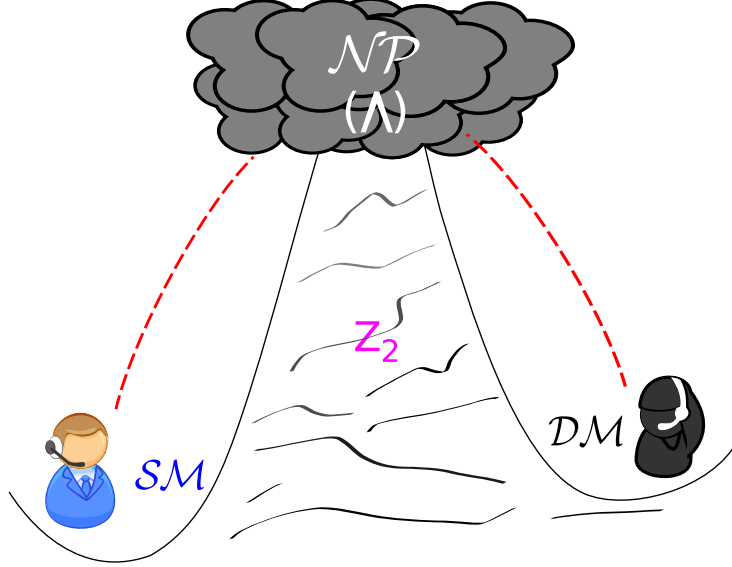


FIG. 1: Pictorial illustration of our EFT model, in which the SM particles interact with the (unknown) DM particles through the new physics which appears at the scale Λ .

in the effective Lagrangian approach have been carried out in the literature [37–46], which focus on different operators.

We add one new field D (the DM candidate) and define the effective Lagrangian as

$$\mathcal{L}_{\text{eff}} = \mathcal{L}_{SM} + \sum \frac{f_i^{(5)}}{\Lambda} \mathcal{O}_i^{(5)} + \sum \frac{f_i^{(6)}}{\Lambda^2} \mathcal{O}_i^{(6)} + \dots, \quad (1)$$

where $\mathcal{O}_i^{(n)}$ is a dimension- n operator which consists of a gauge-invariant combination of the SM and D fields [47, 48]; Λ then denotes the new physics scale (we have assumed that the new physics decouples in the limit $\Lambda \rightarrow \infty$). Since the loop-induced operator suffers from $1/(16\pi^2)$ loop-integration factor, we focus our attention on the tree-level induced operators throughout this work.

The DM candidate field D is assumed to carry an odd quantum number under a discrete Z_2 symmetry¹ under which all SM fields are even. Such a Z_2 symmetry could be an unbroken remnant of some underlying $U(1)$ gauge symmetry [50]. When D is a scalar or fermion, \mathcal{L}_{eff} is then required to be invariant under $SU(3)_c \times SU(2)_L \times U(1)_Y \times Z_2$. When D is a vector, it will be assumed to be the gauge boson of an additional $U(1)_X$ symmetry and to carry

¹ This eliminates possible contributions to observables that are strongly constrained by existing data. For example, if D is a vector field, the Z_2 symmetry forbids contributions to 4-Fermi current-current interactions whose coefficients are tightly bound [49].

no SM quantum numbers; all SM particles are assumed to be $U(1)_X$ singlets and \mathcal{L}_{eff} will be invariant under $SU(3)_c \times SU(2)_L \times U(1)_Y \times U(1)_X$. The main object of this work is to examine the constraints imposed by current DM searches on the coefficients $f_i^{(n)}$. We also explore the collider signatures at the LHC and probe these SM-DM interactions in future DM search experiments.

The rest of this paper is organized as follows. In Sec. II we briefly review some general aspects of dark matter. In Sec. III, IV and V we present our studies of fermionic dark matter, scalar dark matter and vector dark matter, respectively. Finally, in Sec. VI, we review the results of our study and present our conclusions.

II. GENERAL ASPECTS OF COLD DARK MATTER

In order to survive until the present epoch, any dark matter particles must either be stable or have a lifetime longer than the present age of the universe. Furthermore, if the dark matter particles have electromagnetic or strong interactions, they would bind to nucleons and form anomalous heavy isotopes. Such isotopes have been sought but not found [51–53]. Thus, the dark matter particles can, at best, participate in weak (and gravitational) interaction, or, at worst, only participate in gravitational interaction. One obvious possibility satisfying the foregoing constraints is that dark matter consists of neutrinos. However, the present data on neutrino masses show that, although neutrinos might barely account for the inferred DM mass density, they cannot generate the observed structure: simulations of galaxy and cluster formation require the *cold* dark matter. That is, the weakly interacting massive particles (WIMPs) are favored as DM candidates.

The contribution to the energy density from a DM, Ω_{DM} , of mass m_D is [54]

$$\Omega_{DM} h^2 \approx \frac{1.04 \times 10^9}{M_{Pl}} \frac{x_F}{\sqrt{g_*}} \frac{1}{(a + 3b/x_F)}, \quad (2)$$

where $h = 0.73 \pm 0.04$ is the scaled Hubble parameter, $x_F \equiv m_D/T_F$ with T_F being the freeze-out temperature, $M_{Pl} = G_N^{-1/2} = 1.22 \times 10^{19}$ GeV, and g_* counts the number of relativistic degrees of freedom at the freeze-out temperature T_F . As the freeze-out temperature is below the DM mass roughly by a factor of 20-25, the dark matter freeze-out mechanism is independent of the uncertain early thermal history of the universe and possible new interactions at high energy scales. The parameters a and b should be derived from $\langle \sigma v_{rel} \rangle$,

the thermally averaged annihilation cross section of DM (σ) times the relative velocity (v_{rel}), cf. Eq. (A7). The relic abundance of DM in the universe has been precisely measured: combining the results from the WMAP Collaboration with those from the Sloan Digital Sky Survey gives [55]

$$\Omega_{DM}h^2 = 0.111^{+0.011}_{-0.015} \quad (2\sigma \text{ level}). \quad (3)$$

As to be shown below, the accuracy of about 10% in the expected DM abundance imposes an extremely strong bound on the effective operators, and leads to a strong correlation between the dark matter mass and the new physics scale Λ , e.g., the heavier the dark matter the larger the scale Λ . We focus on heavy dark matter, say $m_D \gtrsim 100 \text{ GeV}$, all through this paper and will present the study of the light dark matter elsewhere.

Besides cosmological bounds on dark matter abundance, there are other constraints on the properties of dark matter coming from direct detection searches of WIMPs in the halo of the Milky Way. The idea is that if WIMPs constitute the dominant component of the halo of our galaxy, it is expected that some may cross the Earth at a reasonable rate and can be detected by measuring the energy deposited in a low background detector through the scattering of a dark matter particle with nuclei of the detector. Several experiments have obtained upper bounds on scattering cross sections as a function of WIMP mass. The elastic scattering of a WIMP with nuclei can be separated into spin-independent (SI) and spin-dependent (SD) contributions. SI scattering can take place coherently with all of the nucleons in a nucleus, leading to a cross section proportional to the square of the nuclear mass. As a result, the current constraints on spin-independent scattering are considerably stronger than that on the spin-dependent component. As to be shown, the direct search of dark matter has a significant impact on the effective operators of both fermionic and scalar dark matters.

Additional constraints on relic DM can be derived from the expectation that DM will collect and become gravitationally bound to the center of the galaxy, the center of the Sun and the center of the Earth. If this happens, then a variety of *indirect* dark matter detection opportunities arise. Detecting the annihilation products of dark matter particles in the form of gamma-rays, antimatters and neutrinos are collectively known as indirect search. Among these cosmic-ray observations, gamma-ray is thought to be more robust. Therefore, we focus our attention on the detection of the anomalous cosmic gamma-rays and examine the impact of current measurements and future projected sensitivities on the effective operators.

Studies of antimatter and neutrino searches are also interesting but are beyond the scope of this project.

If the DM particles are light enough, they will be pair-produced at Large Hadron Collider (LHC) and subsequently escape from the detector, resulting in a spectacular collider signature characterized by a large missing transverse momentum. These events can be tagged by requiring that they also contain specific SM particles, such as hard photons, charged leptons, or jets. Extracting the DM signal from this type of events reduces essentially to a counting experiment since a resonance in the invariant mass distribution of the DM particle pair cannot be extracted. Thus, one needs to have better control of the SM background to affirm the existence of DM particles. Here we focus our attention only to the statistical uncertainty of the background events, but needless to say, other uncertainties, such as the systematic error and parton luminosity uncertainty, etc., must be included in order to provide realistic predictions.

Each experiment mentioned above will have different sensitivities to each individual dark operator (i.e. the effective operators) and thus can probe the parameter space of the dark operators independently². Based on the time-line of the experimental programs, it can be achieved in the following steps:

- Current relic abundance measurements severely constrain the dark operators and induce a non-trivial relation between the dark matter mass and the new physics scale.
- Direct and indirect searches of dark matter, mostly the SI scattering experiment, further constrain the parameter space of the dark operators.
- Dark matter pair can be copiously produced at the incoming LHC: discovering events with large missing energy can determine the possible mass of the DM.
- Future direct and indirect detections of dark matter can probe more parameter space lying beyond the reach of LHC.
- Consistently checking all experimental measurements may shed light on the underlying theory.

² Systematic studies of the neutralino dark matter along this direction have been carried out in Refs. [56–58].

The main goal of the remainder of this paper is to show the close connection between dark matter searches and the experiments foreseen at the LHC. We will address this question individually for the fermion, scalar and vector dark matter below.

III. FERMIONIC DARK MATTER χ

We first analyze the case that the DM candidate is a fermion χ , which is assumed to be odd under a Z_2 , and is a SM gauge singlet; we also assume that χ has no chiral interactions. In this case the (tree-level generated) effective interactions with the SM are of two types

- four-fermion:

$$\begin{aligned}\mathcal{O}_{u\chi} &= \frac{1}{2} (\bar{u}\gamma^\mu u) (\bar{\chi}\gamma_\mu\chi), & \mathcal{O}_{d\chi} &= \frac{1}{2} (\bar{d}\gamma^\mu d) (\bar{\chi}\gamma_\mu\chi), \\ \mathcal{O}_{e\chi} &= \frac{1}{2} (\bar{e}\gamma^\mu e) (\bar{\chi}\gamma_\mu\chi), & \mathcal{O}_{\ell\chi} &= (\bar{\ell}\chi) (\bar{\chi}\ell), & \mathcal{O}_{q\chi} &= (\bar{q}\chi) (\bar{\chi}q),\end{aligned}\quad (4)$$

- Vectors, fermions and scalars ³

$$\mathcal{O}_{\phi\chi} = i (\phi^\dagger D_\mu \phi) (\bar{\chi}\gamma_\mu\chi) + h.c. . \quad (5)$$

Here, $q(\ell)$ denotes the left-handed doublets while $u(d, e)$ denotes the right-handed singlet. In the unitary gauge the Higgs doublet is given by

$$\phi = \frac{v+h}{\sqrt{2}} \begin{pmatrix} 0 \\ 1 \end{pmatrix},$$

where h is the SM Higgs boson and $v = 246$ GeV is the vacuum expectation value. All through this study we will choose $m_h = 120$ GeV. With the help of the Fierz identity, the scalar-scalar-current in eq (4) can be written in the vector-vector-current form. In this work, we will focus on the four-fermion effective Lagrangian for the $\bar{\chi}\chi\bar{f}f$ interaction in the form of

$$\mathcal{L}_{\chi f}^{(6)} = \frac{1}{\Lambda^2} (\bar{\chi}\gamma_\mu P_R\chi) \left(\bar{f}\gamma^\mu (g_L^f P_L + g_R^f P_R) f \right), \quad (6)$$

where $f = u, d, e$ and

$$\begin{aligned}g_L^u &= -\frac{1}{2}\alpha_{q\chi}, & g_R^u &= \frac{1}{2}\alpha_{u\chi}, & g_L^d &= -\frac{1}{2}\alpha_{q\chi}, & g_R^d &= \frac{1}{2}\alpha_{d\chi}, \\ g_L^e &= -\frac{1}{2}\alpha_{\ell\chi}, & g_R^e &= \frac{1}{2}\alpha_{e\chi}, & g_L^\nu &= -\frac{1}{2}\alpha_{\ell\chi}, & g_R^\nu &= 0.\end{aligned}\quad (7)$$

³ The dimension-5 operator $\bar{\chi}\chi\phi^\dagger\phi$ has been studied in Refs. [59, 60].

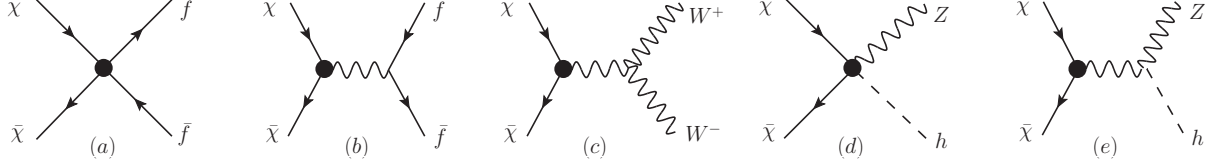


FIG. 2: Feynman diagrams for $\chi\bar{\chi}$ annihilations. Blobs denote the effective vertices induced by the dim-6 operators.

TABLE I: Sensitivities of different experiments to the dark operators where the round brackets denote the Feynman diagrams in Fig. 2 while the square brackets denotes the dark operators. The last three columns denote the LHC collider signatures of those dark operators, $\gamma + \cancel{E}_T$ ($q\bar{q} \rightarrow \gamma\chi\bar{\chi}$), $j + \cancel{E}_T$ ($q\bar{q} \rightarrow j\chi\bar{\chi}$) and $h + \cancel{E}_T$ ($q\bar{q} \rightarrow h\chi\bar{\chi}$); see Fig. 8 for details.

$\Omega_{DM} h^2$	χ -nucleon	cosmic γ -ray \star	$\gamma + \cancel{E}_T$	$j + \cancel{E}_T$	$h + \cancel{E}_T$
(a) $[\alpha_{f\chi}^{L/R}]$	(a) $[\alpha_{f\chi}^{L/R}]$	(a) $[\alpha_{f\chi}^{L/R}]$	(a) $[\alpha_{f\chi}^{L/R}]$	(a) $[\alpha_{f\chi}^{L/R}]$	(d) $[\alpha_{\phi\chi}]$
(d) $[\alpha_{\phi\chi}]$	(b) $[\alpha_{\phi\chi}]$	(d) $[\alpha_{\phi\chi}]$	(b) $[\alpha_{\phi\chi}]$	(b) $[\alpha_{\phi\chi}]$	(e) $[\alpha_{\phi\chi}]$

\star : also sensitive to the sign of the coefficients.

Note that the right-handed projector P_R in eq (6) originates from the fact that the fermionic DM particle considered in this work is a SM gauge singlet. We assume

$$\alpha_{q\chi} = \alpha_{\ell\chi} \equiv \alpha_{f\chi}^L, \quad \alpha_{u\chi} = \alpha_{d\chi} = \alpha_{e\chi} \equiv \alpha_{f\chi}^R,$$

and these operators are also diagonal in the flavor space for simplicity. The fermionic DM can also annihilate into a vector-scalar boson pair via the following vertex:

$$\mathcal{L}_{\chi\phi}^{(6)} = \frac{m_Z}{\Lambda^2} \alpha_{\phi\chi} (\bar{\chi}\gamma^\mu\chi) Z_\mu h. \quad (8)$$

The operator $\mathcal{O}_{\phi\chi}$ also gives rise to the vertex $Z\chi\chi$ as

$$\mathcal{L}_{Z\chi\chi}^{(6)} = \frac{\alpha_{\phi\chi} v m_Z}{2\Lambda^2} Z_\mu \bar{\chi}\gamma^\mu\chi, \quad (9)$$

which contributes to the annihilation processes of $\chi\bar{\chi} \rightarrow Z \rightarrow f\bar{f}$, Zh or W^+W^- . For simplicity we consider the operators $\mathcal{O}_{f\chi}^L$, $\mathcal{O}_{f\chi}^R$ and $\mathcal{O}_{\phi\chi}$ and use the coefficients, $\alpha_{f\chi}^{L/R}$ and $\alpha_{\phi\chi}$, to denote the operators hereafter.

The fermionic DM annihilates into the SM fermions, vector bosons, or into a pair of Higgs boson and Z -boson. The Feynman diagrams of the annihilations are shown in Fig. 2,

where the diagram (a) is related to $\alpha_{f\chi}^{L(R)}$ and the diagrams (b-e) are related to $\alpha_{\phi\chi}$. These five diagrams have different effects on various detection experiments; see Table I. For the annihilation of a heavy χ , the contributions from diagrams (b), (c) and (e), being s -channel processes, are highly suppressed by $1/(4m_\chi^2)$ from the s -channel propagator. Therefore, only diagrams (a) and (d) need to be considered for a heavy χ annihilation. It is worthy mentioning that if χ is very light, say $\sim m_Z/2$, then the diagram (b) receives a large enhancement from the threshold and becomes dominant. Detailed study of such light dark matter will be presented in a future work. For elastic scattering from a nucleus, only diagrams (a) and (b) contribute, whereas for cosmic gamma-ray detection, only diagrams (a) and (d) contribute sizably. Moreover, diagrams (a, b) can be probed at the LHC using the signature of mono-photon plus missing energy while diagrams (d, e) can be probed using the signature of single Higgs scalar plus missing energy, and diagram (c) can be probed using the signal of two forward jets with missing energy. All these issues will be explored in details in the rest of this section.

A. Relic abundance

One can calculate the cross sections of $\chi\bar{\chi}$ annihilation and obtain the leading terms (a and b) in the non-relativistic expansion. The x_F can be determined using Eq. (A8). After substituting x_F and (a , b) into Eq. (2), one can evaluate the relic abundance of the DM. Detailed calculations are given in Appendix B.

The allowed parameter set (m_χ, Λ) with respect to WMAP data is shown in Fig. 3. For a heavy χ , say $m_\chi \gtrsim 300$ GeV, all the SM particles can be treated as massless. One can then obtain the leading terms a and b as follows:

$$a = \frac{m_\chi^2}{\Lambda^4} (0.24\alpha_{f\chi}^{L2} + 0.21\alpha_{f\chi}^{R2} + 0.03\alpha_{\phi\chi}^2), \quad (10)$$

$$b = \frac{m_\chi^2}{\Lambda^4} (0.11\alpha_{f\chi}^{L2} + 0.10\alpha_{f\chi}^{R2} + 0.009\alpha_{\phi\chi}^2). \quad (11)$$

We note that x_F hardly varies, $x_F \simeq 25$ ⁴, in the entire allowed parameter space, but the freeze-out temperature T_F varies from 20 – 80 GeV for $m_\chi \sim 500 - 2000$ GeV. Choosing

⁴ In the equation that determines T_F , x appears in a Boltzmann factor e^{-x} . Taking the logarithm, one can show $x_F \approx 25$ for a wide range of values of the annihilation cross section.

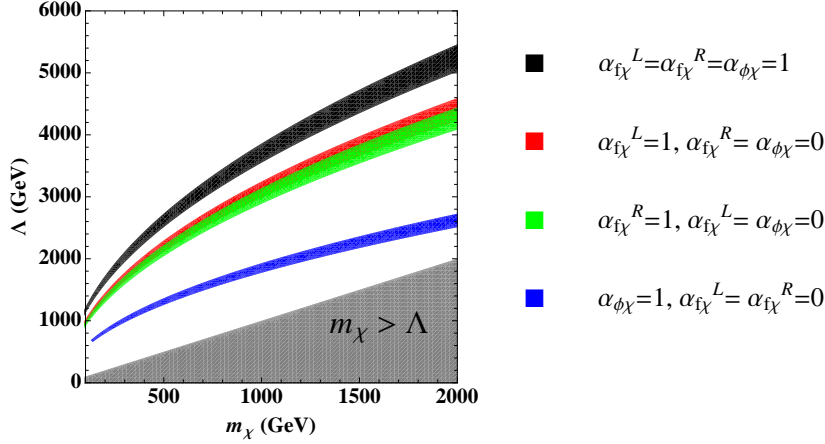


FIG. 3: Allowed parameter set (m_χ, Λ) for a universal coupling constant α when DM is a fermion. The upper (lower) boundary of each band corresponds to the upper (lower) limit of $\Omega_{DM} h^2$.

$x_F = 25$, we obtain the following relation between m_χ and Λ ,

$$\frac{2.22 \times 10^{-2}}{(\Omega_{DM} h^2) (0.252 \alpha_{f\chi}^{L2} + 0.221 \alpha_{f\chi}^{R2} + 0.031 \alpha_{\phi\chi}^2)} = \left(\frac{m_\chi}{100 \text{ GeV}} \right)^2 \left(\frac{\text{TeV}}{\Lambda} \right)^4. \quad (12)$$

We have verified that this relation agrees very well with the numerical results shown in Fig. 3.

For illustrations, we adopt the value of α to be 1 in the following discussions, but it is straightforward to include its effects by rescaling m . When $m_\chi = 500$ GeV, the second lightest new particle is expected to have a mass of about 2 TeV if only $\alpha_{f\chi}^L$ ($\alpha_{f\chi}^R$) is non-zero, but it should appear around 1 TeV if $\alpha_{\phi\chi}$ is present only, see respectively the red (green) and blue bands. The bands of $\alpha_{f\chi}^L$ (red) and $\alpha_{f\chi}^R$ (green) overlap while the $\alpha_{f\chi}^L$ band is slightly higher because the coefficient of $\alpha_{f\chi}^L$ is slightly larger than the one of $\alpha_{f\chi}^R$, see Eq. (12). This small difference comes from three neutrino annihilation channels which only contribute to $\alpha_{f\chi}^L$ but not to $\alpha_{f\chi}^R$. Furthermore, the coefficients of $\alpha_{f\chi}^L$ and $\alpha_{f\chi}^R$ are both larger than the coefficients of $\alpha_{\phi\chi}$ by an order of magnitude, i.e., the annihilation into fermions is dominant in the annihilation cross sections. Eq. (2) implies that, for a given m , the scale Λ has to be small in order to compensate the smaller coefficient of $\alpha_{\phi\chi}$, leading to a much lower band. Finally, when these three couplings all are present, the allowed new physics scale Λ becomes larger, e.g. $\Lambda \sim 2.6 - 5.5$ TeV for $m_\chi \sim 500 - 2000$ GeV.

It is worthy mentioning that for each operator the region below the band is also allowed

even though less relic abundance is produced and additional annihilation channels are needed to explain the current relic abundance.

B. Direct detection of χ

The elastic scattering of a fermion dark matter χ from a nucleus is induced by effective four fermion operators:

$$\begin{aligned}\mathcal{L}_{\chi\chi qq} = & \frac{1}{4\Lambda^2} \left(\alpha_{q\chi}^R - \alpha_{q\chi}^L + \alpha_{\phi\chi} \frac{g}{2\cos\theta_W} \frac{v}{m_Z} C_V^q \right) \bar{\chi} \gamma_\mu \chi \bar{q} \gamma^\mu q \\ & + \frac{1}{4\Lambda^2} \left(\alpha_{q\chi}^R + \alpha_{q\chi}^L + \alpha_{\phi\chi} \frac{g}{2\cos\theta_W} \frac{v}{m_Z} C_A^q \right) \bar{\chi} \gamma_\mu \gamma_5 \chi \bar{q} \gamma^\mu \gamma_5 q,\end{aligned}\quad (13)$$

with $C_V^q = T_3^q - 2Q_q \sin^2 \theta_W$ and $C_A^q = T_3^q$. Here, T_3 and Q are the weak isospin and electric charge of the quark q , respectively, and θ_W is the Weinberg angle. The first term results in a spin-independent scattering from a nucleus while the second term leads to a spin-dependent scattering from a nucleus. It is convenient to consider the cross section with a single nucleon for comparing with experiments.

The DM-nucleus cross section in this case is ⁵

$$\sigma_{\chi N}^{SI} = \frac{m_\chi^2 m_N^2 b_N^2}{\pi (m_\chi + m_N)^2}, \quad (14)$$

where b_N is the effective DM-nucleus coupling. Through simple algebra (see Appendix C 1 for details), we obtain the DM-proton and DM-neutron cross sections as given below:

$$\sigma_{\chi p}^{SI} \approx (6.98 \times 10^{-5} \text{ pb}) \left(\frac{\text{TeV}}{\Lambda} \right)^4 (\alpha_{q\chi}^R - \alpha_{q\chi}^L + 0.013\alpha_{\phi\chi})^2, \quad (15)$$

$$\sigma_{\chi n}^{SI} \approx (6.98 \times 10^{-5} \text{ pb}) \left(\frac{\text{TeV}}{\Lambda} \right)^4 (\alpha_{q\chi}^R - \alpha_{q\chi}^L - 0.162\alpha_{\phi\chi})^2, \quad (16)$$

where $m_\chi \gg m_p \simeq m_n$ are used to derive the approximate results. We note that $\sigma_{\chi p}^{SI} \simeq \sigma_{\chi n}^{SI}$ when either $\alpha_{q\chi}^L$ or $\alpha_{q\chi}^R$ is non-zero, whereas $\sigma_{\chi n}^{SI} \gg \sigma_{\chi p}^{SI}$ when only $\alpha_{\phi\chi}$ presents.

The spin-dependent DM-nuclei elastic scattering cross section can be expressed as

$$\sigma_{\chi N}^{SD} \approx \frac{32m_\chi^2 m_N^2}{\pi (m_\chi + m_N)^2} [\Lambda_N^2 J(J+1)], \quad (17)$$

⁵ Note that Eq. (14) does not correspond to the total DM-nucleus cross section, but to that at zero momentum transfer, usually named as “standard cross section”.

where J is the total angular momentum of the nucleus and $\Lambda_N (\propto 1/J)$ depends on the axial couplings of DM to the quarks. For odd-proton nuclei the spin-dependent DM-nucleus cross section is mainly due to the DM-proton interactions, whereas for odd-neutron nuclei it is dominated by DM-neutron scattering. For even-even nuclei the spin-dependent cross-section is highly suppressed. For the proton/neutron as the target, Eq. (17) is transformed into the cross section from DM-proton/neutron interactions with the proton/neutron spin, which are given as

$$\sigma_{\chi p}^{SD} \approx (4.183 \times 10^{-6} \text{ pb}) \left(\frac{\text{TeV}}{\Lambda} \right)^4 (\alpha_{q\chi}^R + \alpha_{q\chi}^L - 4.53\alpha_{\phi\chi})^2, \quad (18)$$

$$\sigma_{\chi n}^{SD} \approx (4.183 \times 10^{-6} \text{ pb}) \left(\frac{\text{TeV}}{\Lambda} \right)^4 (\alpha_{q\chi}^R + \alpha_{q\chi}^L + 3.53\alpha_{\phi\chi})^2. \quad (19)$$

It indicates that for a given Λ the contribution of $\mathcal{O}_{\phi\chi}$ dominates over the other two operators. Furthermore, we note that $\sigma_{\chi p}^{SD} \approx \sigma_{\chi n}^{SD}$

In Figs. 4(a) and 4(b), we compare the spin-independent elastic scattering cross section of the fermionic DM χ with the current and projected sensitivities of direct detection experiments; the blue-solid curve denotes the XENON10 exclusion limit [61] while the red curve shows the CDMS II 2009 exclusion limit [62]. In the near future, the CDMS II is projected to increase the sensitivities of spin-independent scattering roughly by a factor of 4; see the black-dashed curve. The projected sensitivities of SuperCDMS [63], whose first phase is proposed to start operating in 2011, are also plotted; the blue-dashed line represents phase-A while the red-dashed line phase-C. The red, green and blue bands represent the cross sections for $\alpha_{f\chi}^L = 1$, $\alpha_{f\chi}^R = 1$ and $\alpha_{\phi\chi} = 1$, respectively, with the assumption of only one parameter being non-zero at a time. We note that the bands of $\alpha_{f\chi}^L$ and $\alpha_{f\chi}^R$ overlap for the whole mass range we are interested, whereas the band of $\alpha_{\phi\chi}$ is much higher than those two. It is consistent with the relic abundance constraints shown in Fig. 3. The exclusion limit of m_χ (denoted by the symbol “>”) and the potential reach of future experiments (denoted by “<”) are summarized in Table II. If the recent CDMS II observation is a hint that direct detection is “around the corner”, the the dark matter mass should hide in between the CDMS II 2009 exclusion limit and CDMS II projected sensitivity. Nevertheless, the entire range of m_χ considered here can be covered by the Phase-C of SuperCDMS.

Considering now the case when all three operators contribute, for which the scattering cross sections are shown as the broad gray bands. Although the relic abundance imposes very

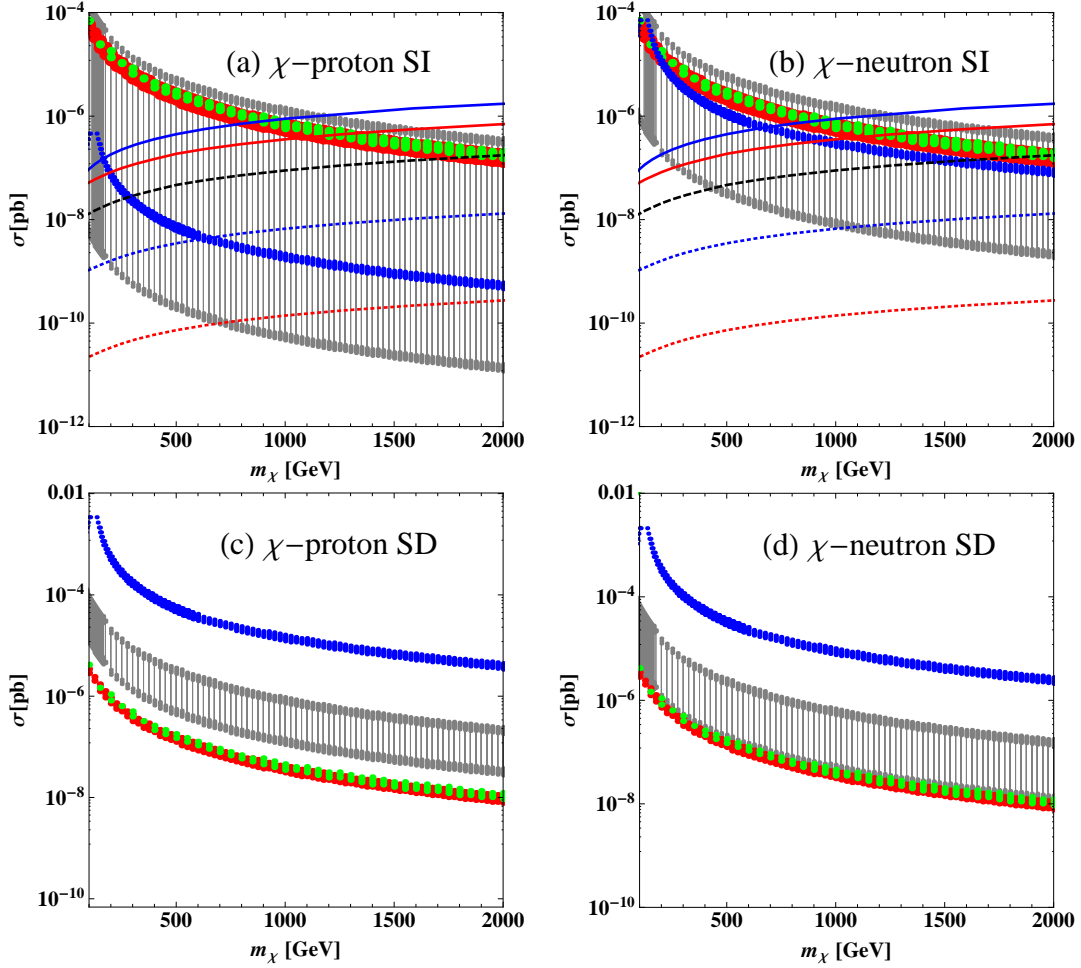


FIG. 4: Prediction of the fermionic DM-nucleon cross sections with respect to m_χ and Λ for allowed parameter set given in Fig. 3; (a, b) for the spin-independent DM search; (c, d) for the spin-dependent DM search. The red (green, blue) band denotes the cross section for $\alpha_{\chi q}^L = 1$ ($\alpha_{\chi q}^R = 1$, $\alpha_{\phi\chi} = 1$), respectively, when one operator is considered at a time. The gray shaded region denotes the cross sections when all these three operators contribute, which corresponds to the black band in Fig. 3; see the text for details. In the upper panel, the blue-solid (red-solid) line labels the upper limit (90% confidence level) on the SI DM-nucleon scattering cross section from the current XENON10 (CDMS II 2009) direct search, respectively. The black-dashed line denotes the near term expected sensitivity from the CDMS II experiment, whereas the blue-dotted (red-dotted) line represents the longer term projection for the Super-CDMS Phase-A (Phase-C), respectively.

TABLE II: Exclusion limits of m_χ (GeV) from current SI direct search (denoted by the symbol “>”) and potential reach of future experiments (denoted by the symbol “<”) when one parameter is considered at a time. The color of each operator refers to Fig. 4.

	XENON10	CDMS II 2009	CDMS II proj	SuperCDMS-A	SuperCDMS-C
$\alpha_{f\chi}^L$ (red)	> 750	> 1050	< 2000	< 2000	< 2000
$\alpha_{f\chi}^R$ (green)	> 800	> 1130	< 2000	< 2000	< 2000
$\alpha_{\phi\chi}$ (blue)	> 600	> 870	< 1700	< 2000	< 2000

tight constraints on m_χ , Λ and the coefficients, see Eq. (12), the signs of the coefficients are not determined as the relic abundance is only proportional to the square of the coefficients. On the contrary, the scattering cross sections are sensitive to the signs of the coefficients; see Eqs. (15-19). The upper limit of the χ -proton SI scattering and the χ -neutron SI scattering corresponds to $\alpha_{f\chi}^L = -\alpha_{f\chi}^R = \alpha_{\phi\chi} = \pm 1$ and $-\alpha_{f\chi}^L = \alpha_{f\chi}^R = \alpha_{\phi\chi} = \pm 1$, respectively. The lower limits of both scattering corresponds to $\alpha_{f\chi}^L = \alpha_{f\chi}^R$, i.e., solely determined by the contribution of $\alpha_{\phi\chi}$. The large difference between two lower limits, for which χ -neutron scattering is much larger than χ -proton scattering, is attributed to the coefficients of $\alpha_{\phi\chi}$ in Eqs. (15) and (16).

For completeness, in Figs. 4(c) and 4(d) we also present spin-dependent cross section which is obviously well below the present and even future experimental reach. Picking out such a signal amongst the large range of noise sources is a considerable challenge. See Ref. [14] for a brief comment on the impact of spin-dependent measurement on the PAMELA antiproton observation.

C. Indirect gamma-ray detection of χ

Photons from dark matter annihilation in the center of the galaxy also provide an indirect signal. Detection of cosmic gamma-rays is carried out in both space-based and ground-based telescopes; the former directly observe the cosmic gamma-rays and can cover the low energy regime (GeV), whereas the latter indirectly observe the gamma-rays through the detection of secondary particles and the Cerenkov light originating from their passage through the Earth’s atmosphere and will cover the high energy regime (100 GeV to TeV). Thus, both types of telescopes can be complementary to each other. The sensitivity of present and

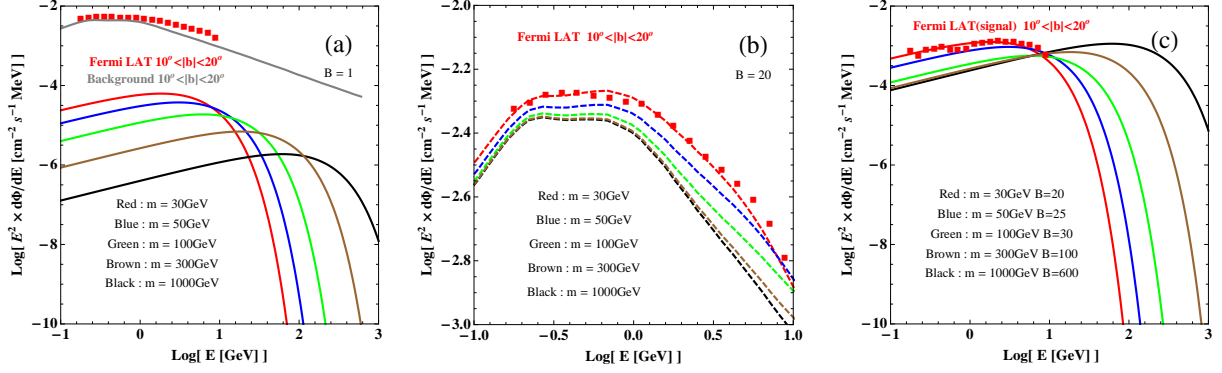


FIG. 5: (a) Predicted gamma-ray spectra for the annihilation of fermionic DM χ (solid lines) with the NFW density profile. The Fermi LAT observation (Galactic background) is also presented by the red-box (grey-solid line); (b) Comparison between the DM signal plus background and the Fermi LAT observation. Note that a common boost factor of 20 is applied to all the DM signals; (c) The comparison between the DM signal with the difference of Fermi LAT observation and background. The different boost factors are adopted for different DM masses so that the DM signal will not exceed the data.

future detectors in gamma-ray astrophysics has been studied in Ref. [64].

As the DM χ cannot annihilate into photon pairs directly, we can only detect continuum photon signals. Using Eq. (D2) we obtain the differential flux of the gamma-rays observed on Earth from DM annihilation as follows:

$$\begin{aligned} \frac{d\Phi}{dE_\gamma} &\approx (1.4 \times 10^{-11} \text{s}^{-1} \text{cm}^{-2} \text{GeV}^{-1}) \bar{J}(\Delta\Omega) \Delta\Omega \\ &\times \left(\frac{100 \text{ GeV}}{m_\chi} \right) \left(\frac{\text{TeV}}{\Lambda} \right)^4 x^{-1.5} e^{-6.5x} (\alpha_{f\chi}^{L2} + \alpha_{f\chi}^{R2} + 0.042 e^{-2.26x} \alpha_{\phi\chi}^2), \end{aligned} \quad (20)$$

where $x \equiv E_\gamma/m_\chi$ and $\bar{J}(\Delta\Omega) \Delta\Omega$ counts the dependence on the DM halo profile (see Appendix D for details). For simplicity, we assume a standard NFW density profile [65, 66] for the DM in our galaxy, i.e. $\bar{J}(\Delta\Omega) \Delta\Omega \sim 1$ for a $\Delta\Omega = 10^{-3}$ sr region around the direction of the galactic center. The predicted differential gamma-ray fluxes from DM annihilation are plotted in Fig. 5(a) with the existing Fermi LAT observations (red box) [67, 68] and the galactic background (gray-solid curve). See Ref. [69] for details of the galactic background and its uncertainties. For illustration, we choose m_χ as 30 (50, 100, 300, 1000) GeV with the corresponding scale Λ which is derived for each mass from the relic abundance, cf. Fig.

3. We only present the distribution of $\alpha_{f\chi}^L = 1$ in the figure as all three operators give rise to almost the same distributions. It is because the shape of gamma-ray spectrum is almost independent of the specific annihilation process and the normalization is also fixed by the relic abundance. Clearly, all flux distributions of the gamma-rays are consistent with the current Fermi LAT observations since the dark matter signals are far below the observation and background.

However, the distribution of dark matter might be clumpy. Such small-scale structure would enhance DM signal by a *boost factor* (B) defined in Eq. (D3). Due to large uncertainties of Galactic background estimations, even there is small discrepancy between signal and background, as shown in Fig. 5, one should not treat such small deviation too seriously. Instead, one can extract upper bounds on the allowed boost factor for dark matter. We vary the boost factor such that the distributions of cosmic gamma-rays for the given m_χ plus background satisfy the Fermi LAT measurement. When the coefficients of the dark operators are set to be 1, we found that a boost factor $B = 20$ is allowed by the Fermi LAT data for the 30 GeV dark matter; see Figs. 5(b) and (c). However, it is in contradiction to the CDMS II observation when one interprets the two events as signal. For a heavier dark matter ($m_\chi > 30$ GeV), the allowed boost factor can be larger. With a large boost factor, such a heavy dark matter would be detected by Fermi LAT with good sensitivity in higher energy region since the dark matter annihilation produces much harder energy spectrum of the cosmic gamma-ray; see Fig. 5(c).

The integrated photon flux is also interesting. The integrated photon flux above some photon energy threshold E_{th} is given by Eq. (D4). We plot the integrated photon fluxes in Fig. 6 as a function of m_χ for two representative E_{th} : 1 GeV, accessible to space-based detectors, and 50 GeV, characteristic of ground-based telescopes. Estimated sensitivities for two promising experiments, Fermi LAT [70] and MAGIC II [71, 72], are also shown. It is clear to see from the Fig. 6 that the Fermi LAT and MAGIC II could probe a heavy χ if the background is well understood.

D. Collider search for χ

Since $x_F \approx 25$ as pointed out above, one can substitute it into the equation of the relic abundance Eq. (2) and obtain the proper thermally averaged annihilation cross section,

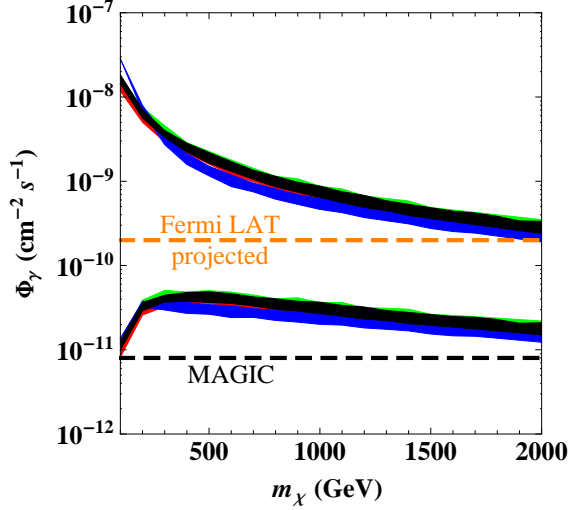


FIG. 6: Integrated photon flux as a function of m_χ for energy threshold of 1 GeV (upper bands) and 50 GeV (lower bands). The notation of the color band is the same as Fig. 4). The plot assumes $\bar{J}(\Psi, \Delta\Omega)\Delta\Omega = 1$; all fluxes scale linearly with this parameter, see the Appendix D for details.

which gives rise to the correct relic abundance, as [73]

$$\langle \sigma_{ann} v_{rel} \rangle \approx 1 \text{ pb.}$$

Inverting the annihilation process, we can produce the DM pair at the LHC though the initial state only consists of light quarks. The $\chi\bar{\chi}$ pair can be produced via the processes

$$q\bar{q} \rightarrow \chi\bar{\chi}, \quad q\bar{q} \rightarrow Z \rightarrow \chi\bar{\chi}, \quad (21)$$

Shown in Fig. 7 is the cross section of the $\chi\bar{\chi}$ pair production (σ_{prod}) as a function of m_χ . The upper narrow band denotes the cross section for $\alpha_{f\chi}^L = 1$ (red), or $\alpha_{f\chi}^R = 1$ (green), or $\alpha_{f\chi}^L = \alpha_{f\chi}^R = \alpha_{\phi\chi} = 1$ (black), whereas the blue narrow band below denotes the cross section for $\alpha_{\phi\chi} = 1$. The upper three narrow bands almost degenerate due to the relic abundance constraints. We note that $\sigma_{prod} \sim 1 \text{ pb}$ for $m_\chi \sim 100 \text{ GeV}$, but σ_{prod} drops steeply with increasing m_χ . The large suppression is due to two facts. The first is the decrease of coupling, since the Λ gets larger. The second reason is due to the parton distribution functions (PDFs) which drop rapidly in the large Bjorken- x region. Typically, $\langle x \rangle \approx 2m_\chi/\sqrt{s}$ with $\sqrt{s} = 14 \text{ TeV}$ for LHC and $\sqrt{s} = 1.96 \text{ TeV}$ for the Tevatron. Such a large suppression restricts the DM search at the LHC to small m_χ . The $\alpha_{\phi\chi}$ operator suffers from a much severer suppression as it contributes only via the Z -boson-exchange process, i.e.

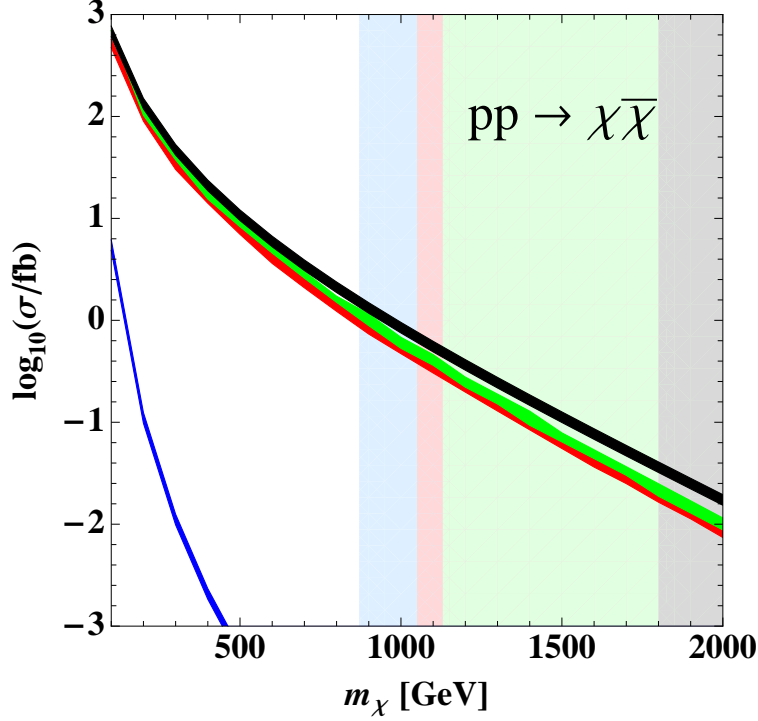


FIG. 7: Cross section of the $\chi\bar{\chi}$ pair production at the LHC. The lower narrow band (blue) denotes the cross section for $\alpha_{\phi\chi} = 1$ while the upper narrow bands (black, green and red) denote the cross sections for $\alpha_{f\chi}^L = 1$, $\alpha_{f\chi}^R = 1$, or $\alpha_{f\chi}^L = \alpha_{f\chi}^R = \alpha_{\phi\chi} = 1$. The shaded regions denote the preferred DM mass region by the CDMS II positive signal; see Table II.

the second term in Eq. (21). For a heavy DM pair, the off-shell Z boson in the propagator receives a large $1/s$ suppression which makes the cross section drop much faster than other bands. The shaded blue (green, red, gray) region denotes the preferred dark matter region for $\alpha_{\phi\chi}$ ($\alpha_{f\chi}^R$, $\alpha_{f\chi}^L$, $\alpha_{f\chi}^L = \alpha_{f\chi}^R = \alpha_{\phi\chi} = 1$) by the CDMS II positive signal.

In order to detect the DM signal, additional SM particles are needed. A hard photon is a good probe which can be produced in association with the DM pair via the following processes

$$q\bar{q} \rightarrow \gamma\chi\bar{\chi}, \quad q\bar{q} \rightarrow Z\gamma \rightarrow \chi\bar{\chi}\gamma, \quad (22)$$

as shown in Fig. 8(a) and (b), giving rise to a collider signature of mono-photon plus large missing transverse momentum ($\gamma + \cancel{E}_T$). Similarly, one can also search for the DM χ using the signature of mono-jet plus missing transverse momentum ($j + \cancel{E}_T$) which involves the

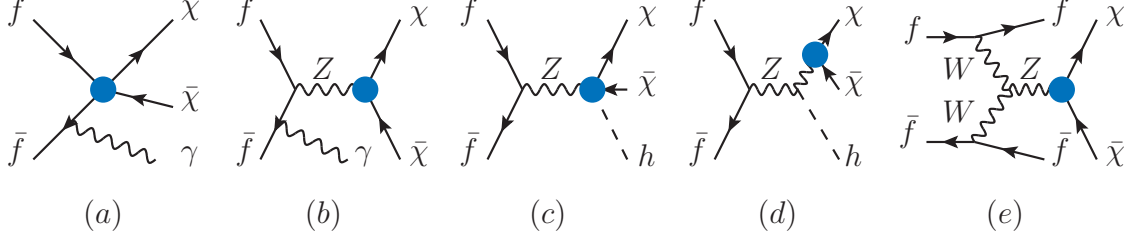


FIG. 8: Schematic diagrams of the searching channels of DM χ at the colliders.

processes as follows:

$$\begin{aligned} q\bar{q} &\rightarrow \chi\bar{\chi}g, & q\bar{q} &\rightarrow Zg \rightarrow \chi\bar{\chi}g, \\ qg &\rightarrow \chi\bar{\chi}q, & qg &\rightarrow Zq \rightarrow \chi\bar{\chi}q. \end{aligned} \quad (23)$$

Furthermore, the $\chi\bar{\chi}$ pair can also be produced associated with a Higgs boson and through the W-boson fusion process, i.e.

$$q\bar{q} \rightarrow Z \rightarrow \chi\bar{\chi}h, \quad q\bar{q} \rightarrow Zh \rightarrow \chi\bar{\chi}h, \quad qq' \rightarrow W^{+*}W^{-*}qq' \rightarrow Z^*qq' \rightarrow \chi\bar{\chi}qq', \quad (24)$$

as shown in Fig. 8(c), (d) and (e). Unfortunately, the cross sections of such processes Eq. (24) are too small to be detected. We then focus our attention on the $\gamma + \cancel{E}_T$ and $j + \cancel{E}_T$ signatures below.

Search for new physics using the collider signatures of $\gamma + \cancel{E}_T$ and $j + \cancel{E}_T$ has been carried out at the Tevatron Run-I ($\sqrt{s} = 1.8$ TeV) and Run II ($\sqrt{s} = 1.96$ TeV), which set upper bounds on the production cross sections of above processes [74, 75]. For the parameter space given in Fig. 3 the production cross section is below the Tevatron direct search bound and is not shown here. We plot the relevant cross sections at the LHC in Fig. 9: (a) $\gamma + \cancel{E}_T$ and (b) $j + \cancel{E}_T$. In Fig. 9(b) we have summed over the processes shown in Eq. (23). Similar to Fig. 7, the lower blue narrow band denotes the cross section for $\alpha_{\phi\chi} = 1$ while the upper narrow bands denote the cross sections for $\alpha_{f\chi}^L = 1$ (red), $\alpha_{f\chi}^R = 1$ (green) and $\alpha_{f\chi}^L = \alpha_{f\chi}^R = \alpha_{\phi\chi} = 1$ (black), respectively. In order to avoid the collinear singularities arising from the light quark propagator, we impose a kinematical cut on the transverse momentum (p_T) of the final state photon or jet as $p_T^{\gamma(j)} \geq 5$ GeV. The shaded regions denote the preferred DM mass region by the CDMS II positive signal (see Table II).

Besides the PDF suppression, the production of the DM pair associated with one single photon (or with one single jet) is suppressed by two additional factors: (i) additional coupling

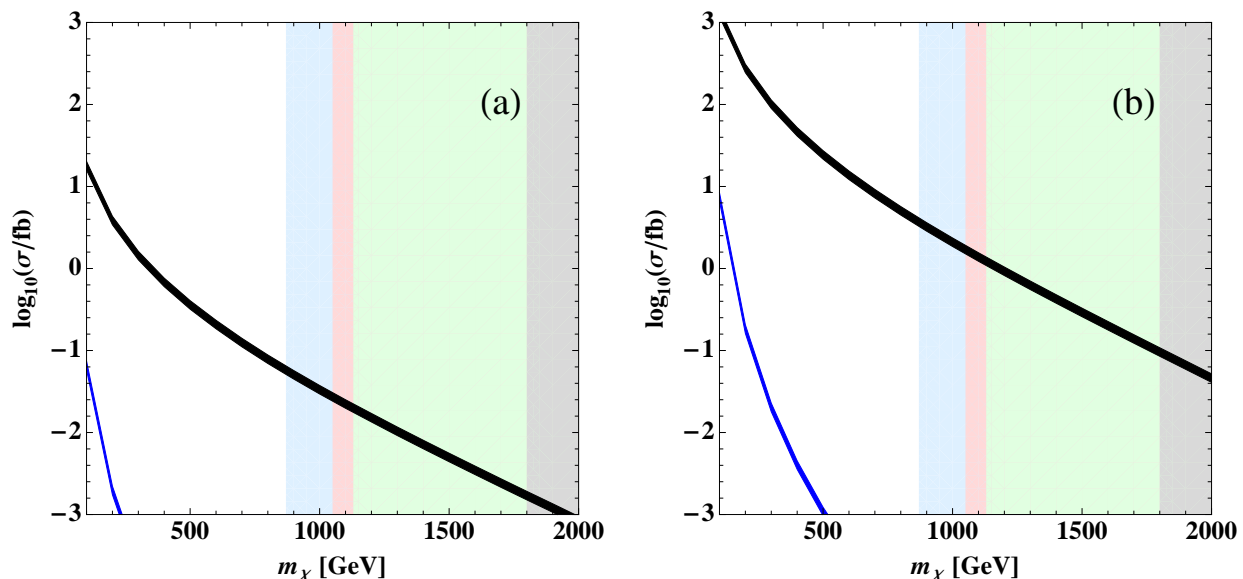


FIG. 9: Production cross sections (in the unit of fb) of the χ pair together with a SM particle at the LHC: (a) mono-photon plus \cancel{E}_T , (b) mono-jet plus \cancel{E}_T , where a kinematics cut $p_T^\gamma > 5$ GeV (or $p_T^j > 5$ GeV) is imposed in order to avoid the collinear singularities arising from the light quark propagators. The lower band (blue) denotes the cross section for $\alpha_{\phi\chi} = 1$ while the upper bands (black, green and red) denote the cross sections for $\alpha_{f\chi}^L = 1$, or $\alpha_{f\chi}^R = 1$, or $\alpha_{f\chi}^L = \alpha_{f\chi}^R = \alpha_{\phi\chi} = 1$. The shaded regions denote the preferred DM mass region by the CDMS II positive signal; see Table II.

(α_{EM} or α_s) and (ii) large volume of three-body phase space. We note that the cross sections of the mono-photon production are much smaller than the ones of the mono-jet production. It is because the former only comes from the quark-quark initial state while the latter comes from both the quark-quark initial state and the quark-gluon initial state. Although having a smaller cross section, the $\gamma + \cancel{E}_T$ process has a relatively clean signature, i.e. hard photon, which could be detected at the LHC. On the other hand, the mono-jet process suffers from huge QCD backgrounds which makes its detection more challenging. Furthermore, the PDFs receive large uncertainties in the large DM mass region, i.e., the large x region. Such large uncertainties will further make the detection of the signal event intricate.

The blue narrow band, i.e. the cross section for $\alpha_{\phi\chi} = 1$, is much lower than other three narrow bands because $\alpha_{\phi\chi}$ only contributes via the Feynman diagram (b) in Fig. 8. Bearing

in mind that Higgs-associated production is also rare, we then conclude that it is hard to observe the *sole* $\alpha_{\phi\chi}$ contribution at the LHC, i.e. one can probe $\alpha_{\phi\chi}$ only via the cosmology observations. For the other operators, the positive CDMS II signal prefers the DM mass $m_\chi \gtrsim 900$ GeV, where the mono-photon and mono-jet production cross sections are of order $\mathcal{O}(10^{-2})$ fb and $\mathcal{O}(1)$ fb, respectively. It is plausible to cross-check the cosmological and collider measurements when the good knowledge of the SM backgrounds and detector sensitivity at the LHC is achieved. For example, see Refs. [40, 42, 45] for a detailed study of bounds from existing Tevatron searches for monojets as well as expected LHC reaches for a discovery.

IV. SCALAR DM φ

Let's now consider the scalar type dark matter. After adding a Z_2 -odd real scalar singlet φ into the SM, we obtain the effective operators as follows:

- scalar only

$$\mathcal{O}_{\phi 1} = \frac{1}{2} (\phi^\dagger \phi)^2 (\varphi\varphi), \quad \mathcal{O}_{\phi 2} = \partial_\mu (\phi^\dagger \phi) \partial^\mu (\varphi\varphi). \quad (25)$$

- scalar-vector

$$\mathcal{O}_{\phi 3} = (\varphi\varphi) (D_\mu \phi^\dagger D^\mu \phi) \quad (26)$$

- scalar fermion

$$\begin{aligned} \mathcal{O}_{e\phi} &= (\varphi\varphi) (\bar{\ell} e \phi), & \mathcal{O}_{u\phi} &= (\varphi\varphi) (\bar{q} u \tilde{\phi}), \\ \mathcal{O}_{d\phi} &= (\varphi\varphi) (\bar{q} d \phi). \end{aligned} \quad (27)$$

Besides the operators listed above, there exists dimension-4 operator $\varphi\varphi\phi^\dagger\phi$ and dimension-5 operator $\varphi\varphi\bar{f}f$ which has been studied in Ref. [60]. There are also a few loop-induced operators which are suppressed by factors of $1/(16\pi^2)$. In this work we only consider the tree-level induced operator, but it is worthy mentioning that those loop-induced operators, e.g. $\varphi\varphi B^{\mu\nu} B_{\mu\nu}$, are also very interesting as they may provide a spectral line feature observable in indirect detection experiments if their contributions dominate in dark matter annihilation [16, 28, 76, 77].

These operators induce the following DM annihilation processes,

$$\varphi\varphi \rightarrow hh, \quad \varphi\varphi \rightarrow VV, \quad \text{and} \quad \varphi\varphi \rightarrow f\bar{f},$$

where $h(V, f)$ denotes the SM Higgs boson (gauge boson, fermion). The vertex of the DM annihilating into the Higgs scalars is

$$\mathcal{L}_{\varphi\varphi hh}^{(6)} = \frac{1}{\Lambda^2} g_{\varphi\varphi hh} \varphi\varphi hh, \quad (28)$$

where

$$g_{\varphi\varphi hh} = \frac{3v^2}{4} \alpha_{\phi 1} + \frac{s}{4} (4\alpha_{\phi 2} + \alpha_{\phi 3}) \quad (29)$$

with s being the square of the system energy. The vertices of the DM annihilating into the vector bosons are summarized as follows,

$$\mathcal{L}_{\varphi\varphi VV}^{(6)} = \frac{1}{\Lambda^2} \left(\alpha_{\phi 3} m_W^2 \varphi\varphi W_\mu^+ W^{-\mu} + \frac{1}{2} \alpha_{\phi 3} m_Z^2 \varphi\varphi Z_\mu Z^\mu \right). \quad (30)$$

The vertices of the DM annihilating into the fermions are

$$\mathcal{L}_{ff}^\varphi = \frac{1}{\Lambda^2} \varphi\varphi \left(\frac{v}{\sqrt{2}} \alpha_{e\phi} \bar{e}_L e_R + \frac{v}{\sqrt{2}} \alpha_{u\phi} \bar{u}_L u_R + \frac{v}{\sqrt{2}} \alpha_{d\phi} \bar{d}_L d_R \right). \quad (31)$$

In this work we consider two possible scenarios of the $\varphi\varphi f\bar{f}$ operators:

- (A) Universal $\alpha_{f\phi}$, i.e. $\alpha_{e\phi} = \alpha_{u\phi} = \alpha_{d\phi}$. As to be shown later, such a case is ruled out by the current DM direct search experiments.
- (B) The coefficients are proportional to the fermion mass, i.e. $\alpha_{f\phi} v = m_f \alpha'_{f\phi}$, and $\alpha'_{f\phi}$ is universal for leptons and quarks, i.e. $\alpha'_{e\phi} = \alpha'_{u\phi} = \alpha'_{d\phi}$. For simplicity, we will use $\alpha_{f\phi}$ instead of $\alpha'_{f\phi}$ hereafter.

Finally, the operator $\mathcal{O}_{\phi 1}$ induces the vertex $\varphi\varphi h$

$$\mathcal{L}_{\varphi\varphi h}^{(6)} = \frac{\alpha_{\phi 1} v^3}{\Lambda^2} \varphi\varphi h, \quad (32)$$

which contributes to the processes of DM annihilation into the SM Higgs bosons, vector bosons and fermions through the Higgs-mediated s -channel processes. In summary, there are four operators contributing to the scalar DM φ annihilation: $\mathcal{O}_{\phi 1}$, $\mathcal{O}_{\phi 2}$, $\mathcal{O}_{\phi 3}$ and $\mathcal{O}_{f\phi}$.

When the scalar φ is the DM, we must consider a large number of annihilation processes, e.g. $\varphi\varphi \rightarrow f\bar{f}/WW/ZZ/hh$ and $\varphi\varphi \rightarrow h \rightarrow f\bar{f}/WW/ZZ/hh$, see Fig. 10. Sensitivities of

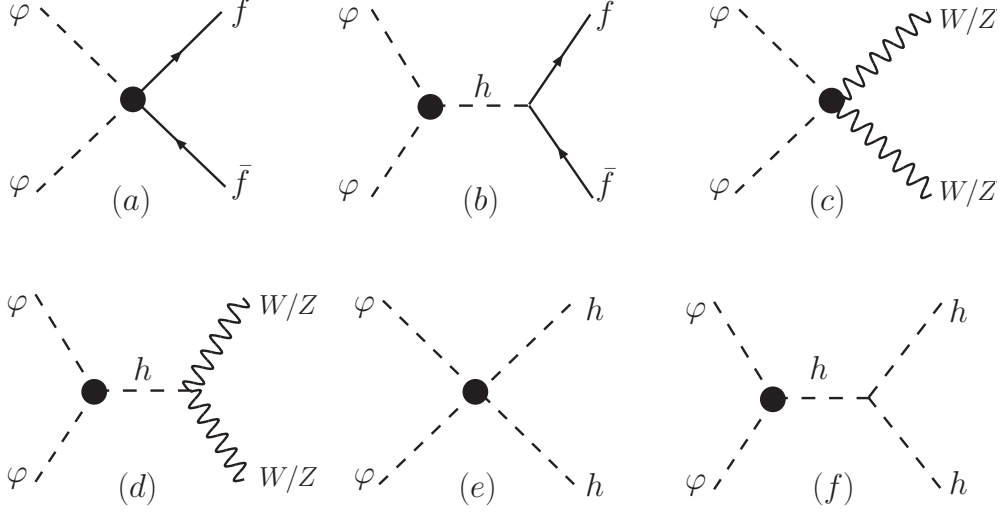


FIG. 10: Feynman diagrams for $\varphi\varphi$ annihilation. Blobs denote the effective vertices induced by the dim-6 operators.

TABLE III: Sensitivities of various experiments to the dark operators where the round brackets denote the Feynman diagrams in Fig. 10 while the square brackets denotes the dark operators given in Eqs. (25-32).

$\Omega_{CDM}h^2$	χ -nucleon	cosmic γ -ray	$\gamma + \cancel{E}_T$	$j + \cancel{E}_T$	VBF
(a) $[\alpha_{f\phi}]$	(a) $[\alpha_{f\phi}]$	(a) $[\alpha_{f\phi}]$	(a) $[\alpha_{f\phi}]$	(a) $[\alpha_{f\phi}]$	(c) $[\alpha_{\phi 3}]$
(c) $[\alpha_{\phi 3}]$	(b) $[\alpha_{\phi 1}]$	(c) $[\alpha_{\phi 3}]$			(d) $[\alpha_{\phi 1}]$
(e) $[\alpha_{\phi 1, \phi 2, \phi 3}]$		(e) $[\alpha_{\phi 1, \phi 2, \phi 3}]$			

these diagrams on various experiments are summarized in Table III. The contributions from the diagrams (b,d,f) are large only around the Higgs resonance region, i.e. $m_\varphi \sim m_h/2$, but for the annihilation of heavy φ pair their contributions are highly suppressed. As we are interested in the region of $m_\varphi > 100$ GeV, only the diagrams (a,c,e) need to be considered. For the elastic scattering from the nucleus, only diagrams (a) and (b) contribute, whereas for the cosmic gamma-ray detection, only diagrams (a,c,e) contribute. Moreover, diagrams (a,b) can be probed at the LHC using the signature of mono-photon plus missing energy while diagrams (c,d) can be probed in the vector-boson-fusion process $q\bar{q} \rightarrow VV q\bar{q} \rightarrow \varphi\varphi q\bar{q}$. Diagrams (e,f) cannot be probed at the LHC.

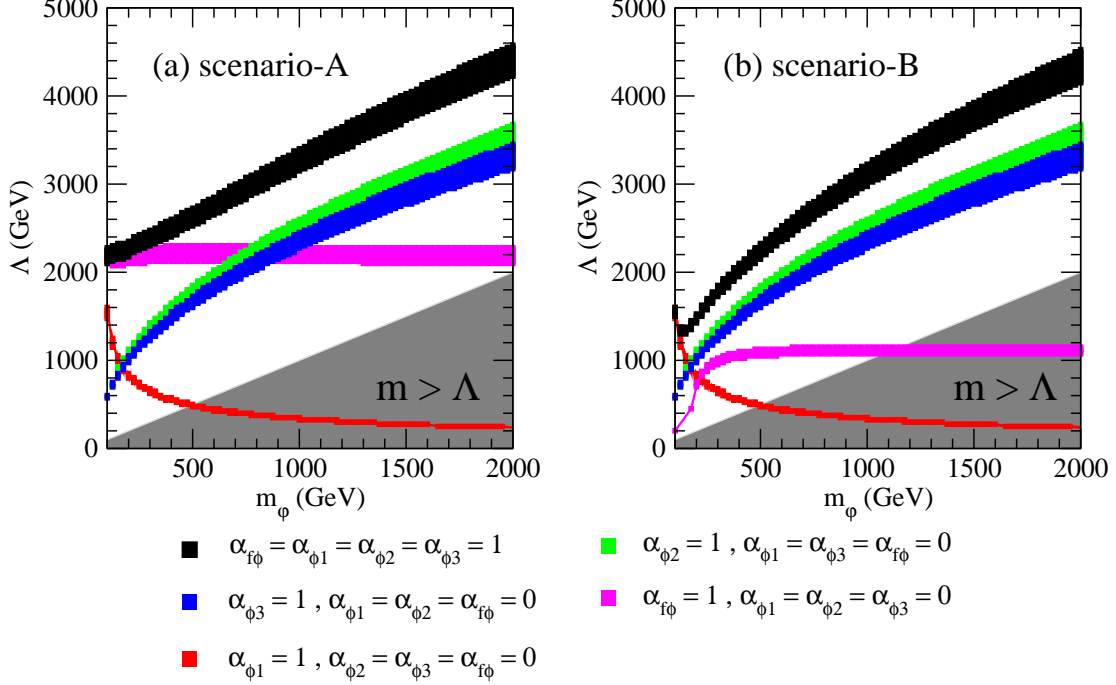


FIG. 11: (a) Allowed parameter set (m_φ, Λ) for the scalar DM φ : (a) scenario-A (family universal coupling); (b) scenario-B (family dependent coupling). The gray shaded region is excluded as $m_\varphi > \Lambda$. The upper (lower) boundary of each band corresponds to the upper (lower) limit of $\Omega_{DM} h^2$ given in Eq. (3).

A. Relic abundance

The scalar DM can annihilate into light fermion pairs, or WW and ZZ pairs if the vector boson channels open. The calculation of the relic abundance is similar to the one of fermion DM χ . We present the annihilation cross sections and the leading terms in the non-relativistic expansion in Appendix B. The allowed parameter space of (m_φ, Λ) is shown in Fig. 11 for both scenario-A and scenario-B.

If the DM annihilation is purely induced by the operator $\mathcal{O}_{\phi 1}$, the scale Λ decreases rapidly with increasing m_φ in order to respect the WMAP data; see the red band. It can be easily understood from dimensional counting as follows. For a heavy m_φ the effective vertices induced by $\mathcal{O}_{\phi 1}$ give rise to the leading terms a and b as following; see Eqs. (B18-B22),

$$a, b \propto \frac{v^4}{m_\varphi^2 \Lambda^4}. \quad (33)$$

Since a and b are fixed by the well-measured relic abundance,

$$\Lambda \propto m_\varphi^{-1/2}, \quad (34)$$

which results in the inverse behavior of the red band. Moreover, m_φ is about equal to the cutoff scale Λ around 500 GeV. We thus conclude that if $\mathcal{O}_{\phi 1}$ is the only source for DM annihilation, then φ should be very light, say $m_\varphi < 500$ GeV. Otherwise, other dark operators have to be considered to explain the relic abundance.

The bound on the operator $\mathcal{O}_{f\phi}$ is not sensitive to m_φ ; see the magenta bands. It can also be understood from dimensional counting. For a heavy φ , the effective vertices induced by $\mathcal{O}_{f\phi}$ give rise to the following leading terms; see Eqs. (B13-B16):

$$a, b \propto \begin{cases} \frac{v^2}{\Lambda^4}, & (\text{scenario - A}), \\ \frac{m_f^2}{\Lambda^4}, & (\text{scenario - B}), \end{cases} \quad (35)$$

therefore, the relic abundance only depends on the scale Λ for both scenarios. We found that for all the mass region concerned, $\Lambda \simeq 2$ TeV in the scenario-A, whereas $\Lambda \simeq 1.1$ TeV for scenario-B. Again in order to satisfy the condition $m_\varphi < \Lambda$, φ cannot be very heavy. For example, m_φ should be less than 1 TeV for scenario-B.

Let's consider now both $\mathcal{O}_{\phi 2}$ and $\mathcal{O}_{\phi 3}$ simultaneously, an interference between them occurs. From the annihilation cross sections given in Eqs. (B17) and (B20), we derive the coefficients in the thermal average taking $m \gg v$ and find

$$a = \frac{m_\varphi^2}{64\pi\Lambda^4} (16\alpha_{\phi 2}^2 + 8\alpha_{\phi 2}\alpha_{\phi 3} + 13\alpha_{\phi 3}^2), \quad (36)$$

$$b = \frac{m_\varphi^2}{256\pi\Lambda^4} (16\alpha_{\phi 2}^2 + 8\alpha_{\phi 2}\alpha_{\phi 3} + 7\alpha_{\phi 3}^2). \quad (37)$$

The allowed parameter set (m_φ, Λ) for each operator is shown in Fig. 11; see the green band ($\alpha_{\phi 2}$) and the blue band ($\alpha_{\phi 3}$). Similar to the case of fermionic DM, we find that x_F barely varies in the entire allowed parameter space, $x_F \simeq 25$, but the freeze-out temperature T_F varies from 20 – 80 GeV for $m_\varphi \sim 500 - 2000$ GeV. Choosing $x_F = 25$, we obtain the following relation between m_φ and Λ ,

$$\frac{6.98 \times 10^{-2}}{(\Omega_{CDM} h^2) (0.273\alpha_{\phi 2}^2 + 0.136\alpha_{\phi 2}\alpha_{\phi 3} + 0.213\alpha_{\phi 3}^2)} = \left(\frac{m_\varphi}{100 \text{ GeV}}\right)^2 \left(\frac{\text{TeV}}{\Lambda}\right)^4. \quad (38)$$

Finally, we consider the case of all the operators contributing to the DM annihilation; see the black band. It is clear that for a heavy φ the DM annihilation is dominated by $\mathcal{O}_{\phi 2}$ and

$\mathcal{O}_{\phi 3}$ given by Eq. (38). Note that the sign of the coefficients $\alpha_{\phi 2}$ and $\alpha_{\phi 3}$ is very important. For simplicity, we only consider the case of constructive interference, i.e., both $\alpha_{\phi 2}$ and $\alpha_{\phi 3}$ being positive, in this study. But one can easily get the result of destructive interference by lowering the black band by $\sim 25\%$. For a light φ , however, the DM annihilation is dominated by $\mathcal{O}_{f\phi}$ in scenario-A while by $\mathcal{O}_{\phi 1}$ in scenario-B.

B. Direct Search

When the DM is a scalar φ , it can be detected in the spin-independent experiments via the scalar interaction with nucleus

$$\mathcal{L}_{\varphi\varphi qq} = \frac{1}{\Lambda^2} \frac{\alpha_{f\phi} v}{\sqrt{2}} \varphi\varphi \bar{q}q + \frac{1}{\Lambda^2} \frac{\alpha_{\phi 1} v^2}{2} \frac{m_q}{m_h^2} \varphi\varphi \bar{q}q, \quad (39)$$

which leads to a total spin-independent φ -nucleon cross section as follows:

$$\sigma_{\varphi p}^{SI} = \frac{m_p^2}{4\pi (m_\varphi + m_p)^2} [f_{\varphi p}^{(p)}]^2, \quad \sigma_{\varphi n}^{SI} = \frac{m_n^2}{4\pi (m_\varphi + m_n)^2} [f_{\varphi n}^{(n)}]^2, \quad (40)$$

where the effective φ -nucleon couplings, $f_{\varphi p}^{(p)}$ and $f_{\varphi n}^{(n)}$, are given in Appendix C 2. In practice, we found $\sigma_{\varphi p}^{SI} \simeq \sigma_{\varphi n}^{SI}$.

The SI elastic φ -nucleon scattering cross sections are plotted in Fig. 12 along with the current limits placed by the CDMS II 2009 (red-solid) and XENON10 (blue-solid) collaborations, the projected CDMS II sensitivity (black-dashed), and the projected future sensitivity of SuperCDMS, Stage-A (blue-dotted) and Stage-C (black-dotted). If the scalar DM annihilation occurs purely through the $\mathcal{O}_{\phi 1}$ operator (see the red band), then the current direct detection from CDMS and XENON has no constraint on the DM as the elastic scattering cross section is far below the current bounds, almost by two order of magnitude. However, the operator can be probed completely in the projected future SuperCDMS at Stage-C. One should keep in mind that the mass of φ should be less than 500 GeV, otherwise the mass of φ is larger than the NP scale Λ . However, the positive CDMS II would rule out $\mathcal{O}_{\phi 1}$ when the DM signal is observed in the near future.

The magenta band shows the cross section for $\alpha_{f\phi} = 1$. Consider scenario-A first. The cross section is so large that the entire parameter space $100 \text{ GeV} \leq m_\varphi \leq 2 \text{ TeV}$ is excluded by the CDMS and XENON data. If all the operators contribute to the DM annihilation, the relic abundance allowed scale Λ becomes large so that the SI scattering cross section is

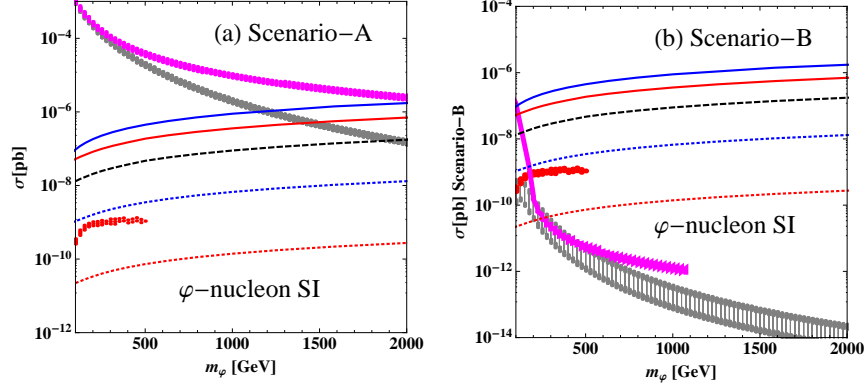


FIG. 12: SI φ -nucleon scattering cross sections as a function of m_φ . The red band represents the cross section for $\alpha_{\phi 1} = 1$, the magenta band denotes the cross section for $\alpha_{f\phi} = 1$, and the gray band denotes the cross section for $\alpha_{f\phi} = \alpha_{\phi 1} = \alpha_{\phi 2} = \alpha_{\phi 3} = 1$. See Fig. 4 for description of other curves.

suppressed, see the gray band. The CDMS and XENON measurements excluded the region of $m_\varphi \leq 1450$ GeV, and the projected CDMS II sensitivity covers m_φ up to 2000 GeV. On the contrary, in scenario-B, the SI scattering cross section is well below the current CDMS and XENON data. Even the long-term SuperCDMS at Stage-C can only probe m_φ up to 300 GeV. Similar to the case of fermion DM χ , the broad gray band is due to the different sign assignments of $\alpha_{f\phi}$ and $\alpha_{\phi 1}$. Hence, we find following interesting points:

1. When the CDMS II observe dark matter signal in the near future, the dark matter in the scenario-A (family universal coupling) lie between the mass window (1450 GeV - 2000 GeV) when $\alpha_{f\phi} = \alpha_{\phi 1} = \alpha_{\phi 2} = \alpha_{\phi 3} = 1$. The dark matter in the scenario-B (family dependent coupling), however, is very light, say $100 \text{ GeV} < m_\varphi < 150 \text{ GeV}$ with $\Lambda \sim \text{TeV}$.
2. When no dark matter signal is observed within the projected CDMS II sensitivity, the scenario-A is almost excluded for $m_\varphi < 2 \text{ TeV}$. However, most of the parameter space of scenario-B is still allowed and is hard to probe even with the long-term SuperCDMS at Stage-C.

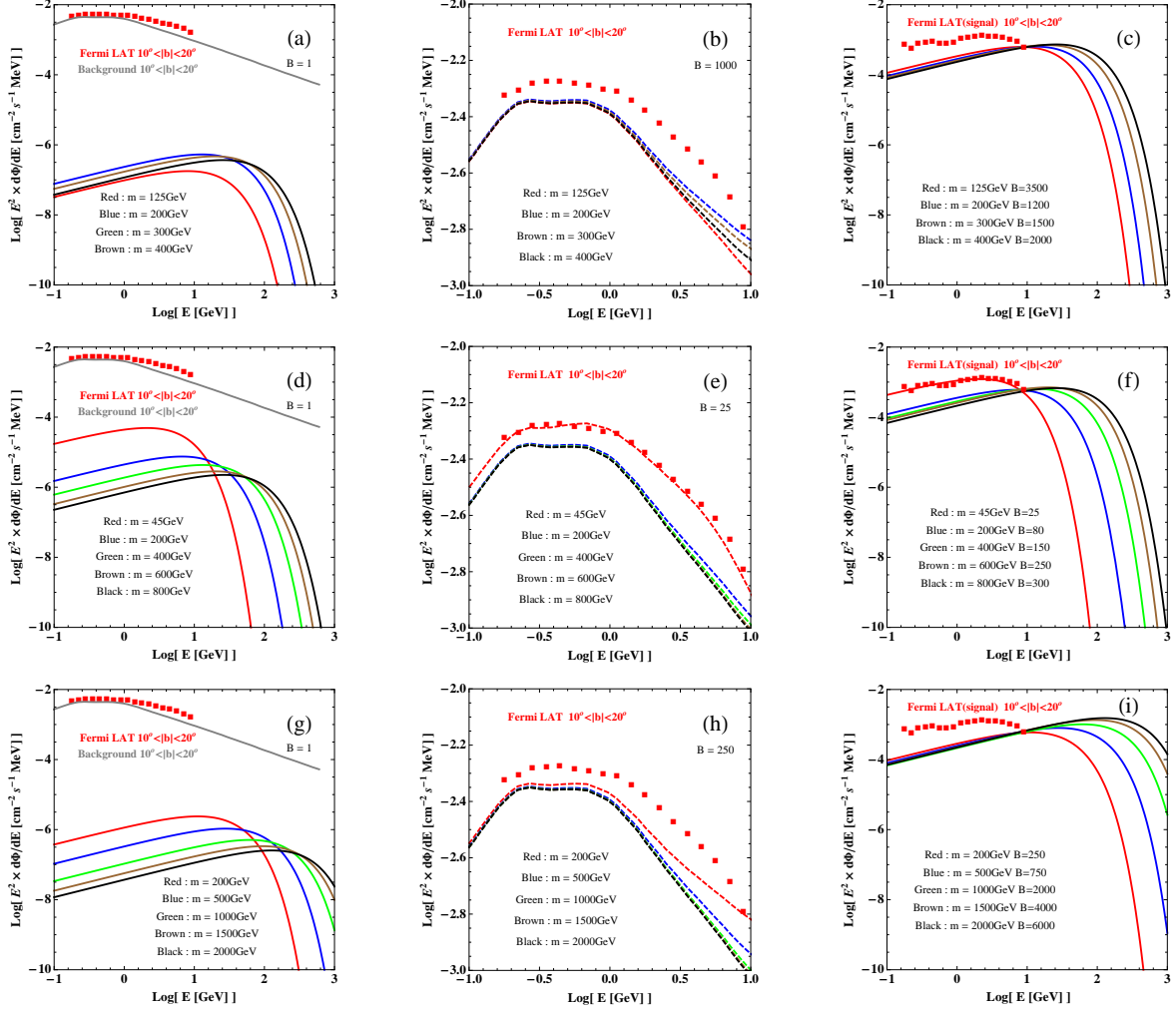


FIG. 13: Predicted gamma-ray spectra for the scalar DM φ with the NFW density profile: (a, b, c) $\alpha_{\phi 1} = 1$, (d, e, f) $\alpha_{f\varphi} = 1$, and (g, h, i) $\alpha_{\phi 2} = 1$ or $\alpha_{\phi 3} = 1$ or $\alpha_{\phi 1} = \alpha_{\phi 2} = \alpha_{\phi 3} = \alpha_{f\varphi} = 1$. The left panel shows the predicted gamma-ray spectra for the scalar DM φ . The middle panel shows the the summed gamma-ray spectra of signal plus background with the Fermi LAT observation. Note that a common boost factor is applied to all the DM signals. The right panel shows the DM signal with the difference of Fermi LAT observation and background. Different boost factors are adopted for different DM masses so that the DM signal will not exceed the data.

C. Indirect search

We now consider the indirect search of φ via cosmic gamma-rays. As most of the parameter space of scenario-A is excluded, we focus on scenario-B hereafter. Similar to the fermionic dark matter in previous section, we plot the differential distribution of the gamma-

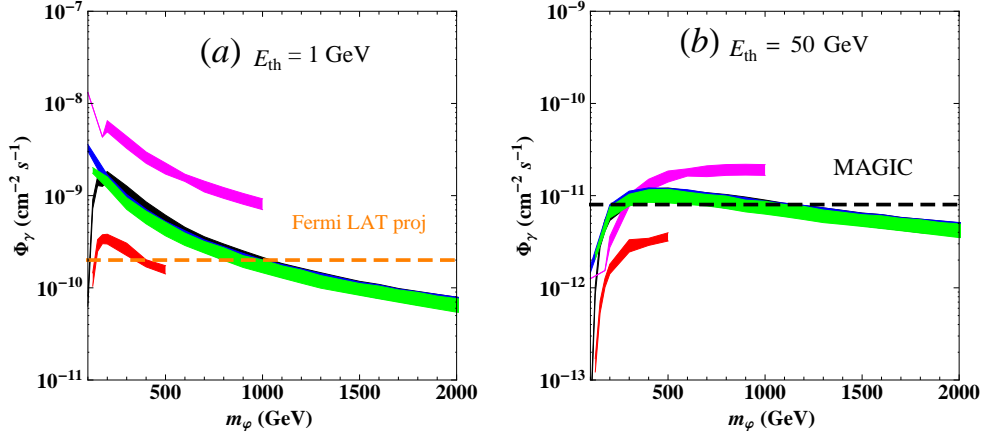


FIG. 14: Integrated photon flux as a function of m_ϕ for energy threshold of 1 GeV (a) and 50 GeV (b) (notation of the color bands is the same as Fig. 11). The plot assume $\bar{J}(\Psi, \Delta\Omega) \Delta\Omega = 1$; all fluxes scale linearly with this parameter.

ray flux for various scalar DM masses and boost factors in Fig. 13. Figs. (a, b, c) shows the distributions of $\alpha_{\phi 1} = 1$; Figs. (d, e, f) display the distributions of $\alpha_{f\phi} = 1$; Figs. (g, h, i) denote the distributions of $\alpha_{\phi 2} = 1$, or $\alpha_{\phi 3} = 1$, or $\alpha_{\phi 1} = \alpha_{\phi 2} = \alpha_{\phi 3} = \alpha_{f\phi} = 1$ as their distributions are almost the same. It is clear that the allowed boost factors for the operator $\alpha_{f\phi}$ is much smaller than that for $\alpha_{\phi 1}$ and $\alpha_{\phi 2}$ (or $\alpha_{\phi 3} = 1$, or $\alpha_{\phi 1} = \alpha_{\phi 2} = \alpha_{\phi 3} = \alpha_{f\phi} = 1$).

The integrated cosmic photon-flux as a function of m_D is plotted in Fig. 14. We choose two energy thresholds $E_{th} = 1$ GeV and $E_{th} = 50$ GeV to mimic the space-based and ground-based telescopes. For simplicity we assume $\bar{J}(\Delta\Omega) \Delta\Omega = 1$ and all the fluxes scale linearly to account for other DM density profiles. Fermi LAT and MAGIC have great potential to observe anomalous gamma-rays. With an enhancement factor, say ~ 10 , from either the DM density profile or the boost factor, almost all the allowed mass region (100 GeV – 2000 GeV) can be explored by Fermi LAT and MAGIC.

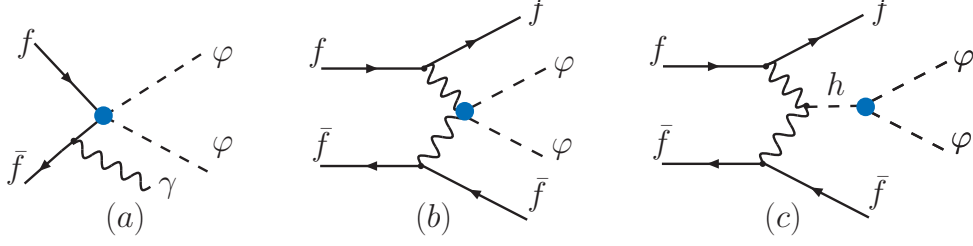


FIG. 15: Schematic diagrams of the searching channels of DM χ at the colliders.

D. Collider search

Now consider the direct search of φ at the LHC. The scalar DM φ can be detected in the following processes

$$q\bar{q} \rightarrow \gamma\varphi\varphi, \quad (41)$$

$$q\bar{q} \rightarrow VVq'q' \rightarrow q'q'\varphi\varphi, \quad (42)$$

where the former is from the four-particle interaction; see Fig. 15(a), while the latter is from the so-called vector boson fusion (VBF) process; see Fig. 15(b) and (c).

The collider signature of the process in Eq. (41) consists of a hard photon plus large \cancel{E}_T due to the missing DM particles. Furthermore, φ can also be probed with a collider signature of a mono-jet plus large \cancel{E}_T . The corresponding processes are as follows:

$$q\bar{q} \rightarrow g\varphi\varphi, \quad gg \rightarrow q\varphi\varphi.$$

The signal of the VBF process is characterized by two quark jets, which typically stay in the forward and backward regions of the detector and are widely separated in pseudo-rapidity, and also by a large missing transverse momentum (\cancel{E}_T), due to the two missing DM particles.

In Fig. 16 we plot the cross sections of the above processes as a function of m_φ with the corresponding Λ consistent with the DM relic abundance. As only $\mathcal{O}_{\phi 1}$ and $\mathcal{O}_{f\phi}$ operators can contribute to the signatures of $\gamma + \cancel{E}_T$ and $j + \cancel{E}_T$, we plot their effects separately in Fig. 16 (a) and (b) where the red curve denotes $\mathcal{O}_{\phi 1}$ while the magenta curve denotes $\mathcal{O}_{f\phi}$. Although both $\mathcal{O}_{\phi 3}$ and $\mathcal{O}_{f\phi}$ are involved in the VBF process, the latter contributes much less than the former, especially for a heavy φ . Therefore, we only present the cross section of $\mathcal{O}_{\phi 3}$ in Fig. 16(c). We note that the cross sections are generally small for all the processes. Note also that various kinematics cuts are needed in order to suppress the SM background.

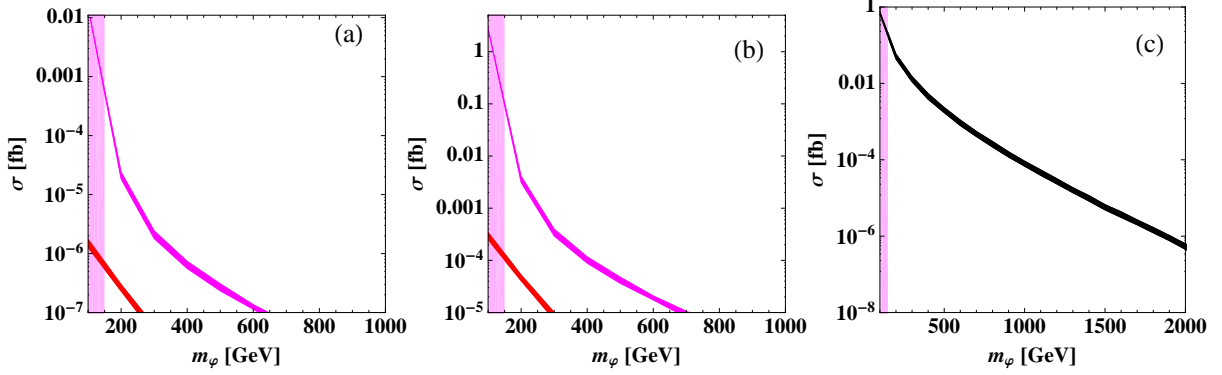


FIG. 16: Production cross sections (in the unit of fb) of the φ pair together with a SM particle at the LHC: (a) mono-photon plus \cancel{E}_T , (b) mono-jet plus \cancel{E}_T , and (c) VBF. Here, a kinematics cut $p_T^\gamma > 5 \text{ GeV}$ (or $p_T^j > 5 \text{ GeV}$) is imposed in order to avoid the collinear singularities arising from the light quark propagators. In (a) and (b), the lower band (red) denotes the cross section for $\alpha_{\phi 1} = 1$ while the upper bands (magenta) denotes the cross section for $\alpha_{f\phi} = 1$. The shaded regions denote the preferred DM mass region by the CDMS II positive signal.

We hence conclude that it is very challenging to directly detect the DM φ signal through those processes at the LHC.

V. VECTOR DARK MATTER \mathcal{Z}

The DM candidate can also be a vector boson. In this work we consider a simple extension of the SM electroweak gauge group, i.e. adding an Abelian gauge group $U(1)_X$ to the SM gauge group, extending it to $SU(2)_L \times U(1)_Y \times U(1)_X$. Note that the $SU(2)_L \times U(1)_Y \times U(1)_X$ is only an effective theory below the scale Λ where other fields which interact with both the SM and the $U(1)_X$ in the underlying theory decouple. The Abelian vector field for the $U(1)_X$ is denoted as \mathcal{Z} with a field strength $C_{\mu\nu} \equiv \partial_\mu \mathcal{Z}_\nu - \partial_\nu \mathcal{Z}_\mu$. We further assume that the quarks, leptons and the Higgs field of the SM do not carry $U(1)_X$ quantum numbers, and the field \mathcal{Z} does not carry quantum numbers of the SM gauge group so that it can be the DM candidate.

We can write down the following dim-6 effective operator

$$\mathcal{O}_{\phi\mathcal{Z}} = \frac{1}{2} (\phi^\dagger \phi) C_{\mu\nu} C^{\mu\nu},$$

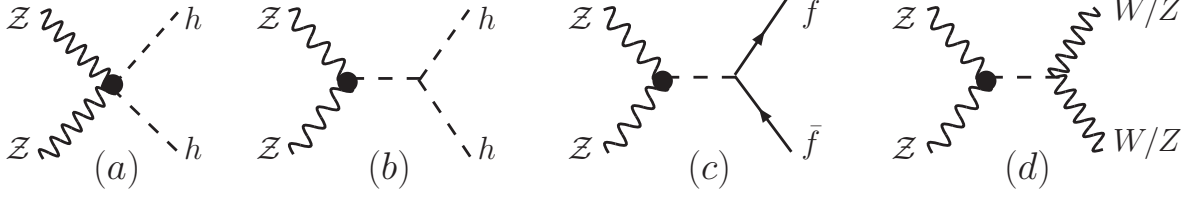


FIG. 17: Feynman diagrams for $\mathcal{Z}\mathcal{Z}$ annihilation. Blobs denote the effective vertices induced by the dim-6 operators.

which induces the $\mathcal{Z}\mathcal{Z} \rightarrow hh$ annihilation via the following vertices

$$\mathcal{L}_{\mathcal{Z}\mathcal{Z}hh}^{(6)} = \frac{\alpha_{\phi\mathcal{Z}}}{4\Lambda^2} hh C_{\mu\nu} C^{\mu\nu}, \quad \mathcal{L}_{\mathcal{Z}\mathcal{Z}h}^{(6)} = \frac{\alpha_{\phi\mathcal{Z}} v}{2\Lambda^2} h C_{\mu\nu} C^{\mu\nu}.$$

In the dimension-six operator, the vector DM \mathcal{Z} can either directly annihilate into the Higgs boson pair or annihilate via the Higgs-mediated s -channel process into the fermion, Higgs boson and vector boson pair; see Fig. 17. It is much simpler as only one operator is present now. Needless to say, for a heavy \mathcal{Z} , the diagram Fig. 17(c) is negligible.

A. Relic abundance

Since the cross section of $\mathcal{Z}\mathcal{Z} \rightarrow f\bar{f}$ is proportional to the fermion mass square, only the top quark can contribute significantly to the DM annihilation. When the DM \mathcal{Z} is light, say $80 \text{ GeV} < m < 150 \text{ GeV}$, it predominantly annihilates into the vector bosons. In the very heavy limit, i.e. $m \gg m_t$, the DM \mathcal{Z} will annihilate into WW , ZZ and Higgs boson pairs, giving rise to the following simple form of a and b ,

$$a = \frac{39\alpha_{\phi\mathcal{Z}}^2 m^2}{256\pi\Lambda^4}, \quad b = \frac{169\alpha_{\phi\mathcal{Z}}^2 m^2}{2048\pi\Lambda^4}. \quad (43)$$

We calculate the relic abundance and plot the allowed parameter space of $(m_{\mathcal{Z}}, \Lambda)$ in Fig. 18; for instance, $\Lambda \simeq 700 \text{ GeV}$ for $m_{\mathcal{Z}} \simeq 100 \text{ GeV}$ while $\Lambda \simeq 3000 \text{ GeV}$ for $m_{\mathcal{Z}} \simeq 2000 \text{ GeV}$. Again, since x_F barely changes in the whole region, we choose $x_F = 25$ and obtain an interesting relation between m and Λ as follows:

$$\frac{0.43}{\alpha_{\phi\mathcal{Z}}^2 (\Omega_{CDM} h^2)} = \left(\frac{m}{100 \text{ GeV}} \right)^2 \left(\frac{\text{TeV}}{\Lambda} \right)^4, \quad (44)$$

which agrees with the exact scanning results shown in Fig. 18. But such a simple relation is no longer valid when the SM Higgs boson is very heavy because of the large enhancement at the threshold $m_{\mathcal{Z}} \approx m_h/2$.

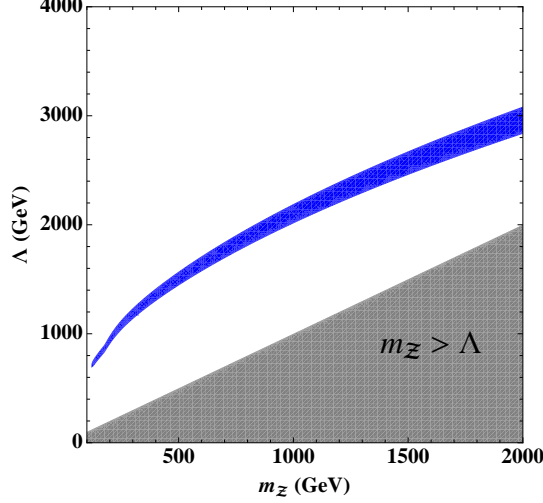


FIG. 18: Allowed parameter set (m_Z, Λ) for a vector DM Z . The upper (lower) boundary of each band corresponds to the upper (lower) limit of $\Omega_{DM} h^2$ given in Eq. (3).

B. Direct Detection

Since the vector DM Z only interacts with the SM Higgs boson in our model, it can be detected in spin-independent experiments. The relevant Lagrangian is given by

$$\mathcal{L}_{ZZqq} = \frac{\alpha_{\phi Z}}{2\Lambda^2} \frac{m_q}{m_h^2} C_{\mu\nu} C^{\mu\nu} \bar{q}q, \quad (45)$$

which gives rise to the effective Z -nucleon cross sections σ_{Zp}^{SI} and σ_{Zn}^{SI} as follows:

$$\sigma_{Zp}^{SI} = \sigma_{Zn}^{SI} \approx (2.88 \times 10^{-10} \text{ pb}) \alpha_{\phi Z}^2 \left(\frac{m_Z}{100 \text{ GeV}} \right)^2 \left(\frac{\text{TeV}}{\Lambda} \right)^4 \left(\frac{100 \text{ GeV}}{m_h} \right)^4. \quad (46)$$

The SI elastic Z -nucleon scattering cross sections are plotted in Fig. 19 for three choices of the SM Higgs boson mass, along with the projected future sensitivity of SuperCDMS Stage-A (blue dashed line) and Stage-C (red dashed curve). The cross sections are well below all the current bounds from CDMS collaboration, but can be probed at the future SuperCDMS experiment at Stage-C. The almost flat behavior of the black band can be easily understood from Eqs. (44) and (46) as

$$\sigma_{Zp}^{SI} \propto \alpha_{\phi Z}^2 \left(\frac{m_Z}{100 \text{ GeV}} \right)^2 \left(\frac{\text{TeV}}{\Lambda} \right)^4 \propto \frac{1}{\Omega_{CDM} h^2}. \quad (47)$$

Since σ_{Zp}^{SI} does not depend upon m_Z , one can not determine m_Z from the SuperCDMS experiment even if such an excess is indeed observed. But it might be possible to measure

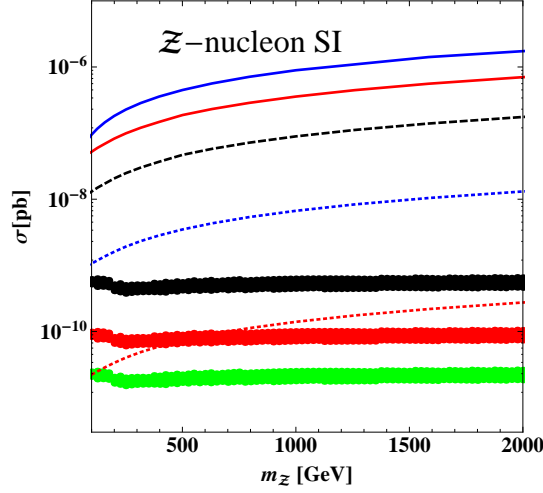


FIG. 19: Vector WIMP-nucleon cross sections for spin-independent dark matter search. The shaded region is our parameter space which respects the observed WMAP data for $\alpha_{\phi Z} = 1$: the black band for $m_h = 120$ GeV, the red band for $m_h = 300$ GeV, and the green band for $m_h = 600$ GeV. See Fig. 4 for descriptions of other curves.

m_Z via indirect cosmic gamma-ray measurements as discussed below. Needless to say, the positive signal of CDMS II would exclude the possibility of vector dark matter.

C. Indirect search

The differential cosmic gamma-ray distribution is given by

$$\begin{aligned} \frac{d\Phi}{dE_\gamma} &\approx (0.76 \times 10^{-12} \text{s}^{-11} \text{cm}^{-2} \text{GeV}^{-1}) \bar{J}(\Psi, \Delta\Omega) \Delta\Omega \\ &\times \alpha_{\phi Z}^2 \left(\frac{100 \text{ GeV}}{m_\chi} \right) \left(\frac{\text{TeV}}{\Lambda} \right)^4 x^{-1.5} e^{-7.76x}. \end{aligned} \quad (48)$$

We plot the differential distributions as a function of E_γ in Fig. 20(a) for various m_Z with the NFW density profile. For $m_Z \sim 100 - 2000$ GeV the distributions are well below the current Fermi LAT data. The discovery of the dark matter signal could be possible in the high energy region after including an allowed boost factor; see Figs. 20(b) and (c).

We plot the integrated cosmic photon-flux as a function of m_Z in Fig. 21. Similar to the study of the fermion and scalar DM, we choose two energy thresholds $E_{th} = 1$ GeV and $E_{th} = 50$ GeV to mimic the space-based and ground-based telescopes. Assuming $\bar{J}(\Psi, \Delta\Omega) \Delta\Omega = 1$

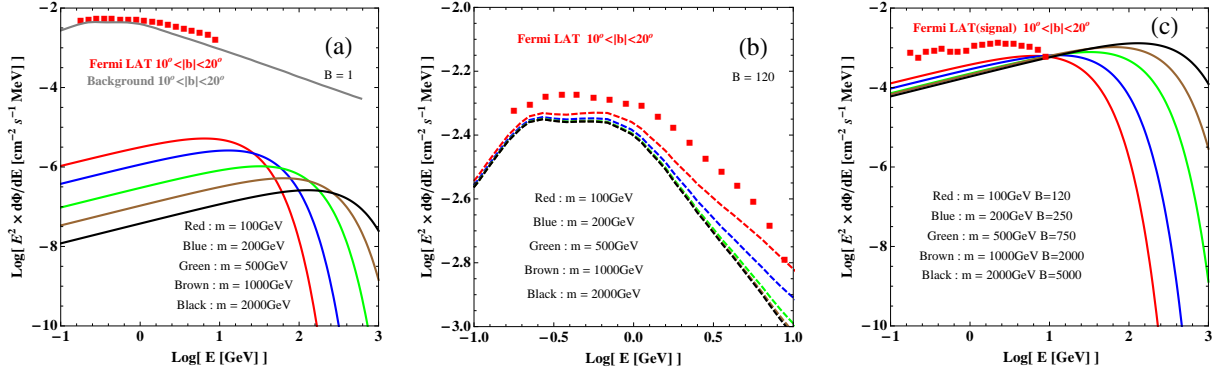


FIG. 20: (a) Predicted gamma-ray spectra for the DM \mathcal{Z} with the NFW density profile, where the Fermi LAT observation (background) is presented by the red-box (grey-solid) line; (b) Comparison between the DM signal plus background and the Fermi LAT observation. Note that a common boost factor of 120 is applied to all the DM signals; (c) The comparison between the DM signal with the difference of Fermi LAT observation and background. Different boost factors are adopted for different DM masses so that the DM signal will not exceed the data.

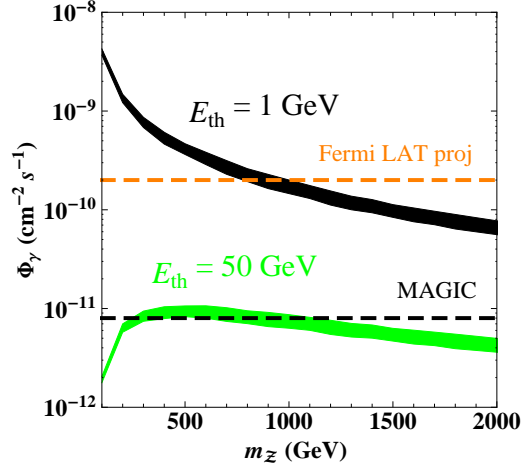


FIG. 21: Integrated photon flux as a function of $m_{\mathcal{Z}}$ for energy threshold of 1 GeV (a) and 50 GeV (b) (notation of the color bands is the same as Fig. 18). The plot assumes $\bar{J}(\Psi, \Delta\Omega) \Delta\Omega = 1$; all fluxes scale linearly with this parameter.

and without the boost factor effect, Fermi LAT can probe $m_{\mathcal{Z}} \sim 100 \text{ GeV} - 1000 \text{ GeV}$ while MAGIC can probe $m_{\mathcal{Z}} \sim 250 \text{ GeV} - 1000 \text{ GeV}$.

D. Collider search

The detection of the vector \mathcal{Z} can be probed in the VBF process at the LHC as \mathcal{Z} only interacts with the SM Higgs boson. The production process is given by

$$q\bar{q} \rightarrow q\bar{q}VV \rightarrow q\bar{q}\mathcal{Z}\mathcal{Z}.$$

The cross section of the production is plotted in Fig. 22, which is too small to be detected at the LHC.

VI. CONCLUSION

Despite its great success, the Standard Model of particle physics needs to be extended to explain the dark matter observation. So far many new physics models have been introduced to address DM physics, but our knowledge of the DM candidate is still subject to cosmological observations. For example, the properties of the DM candidate, e.g., its mass and spin, remain mysterious. In this work we present a model-independent study of DM physics using effective field theory. We add to the SM a new DM field D whose stability is guaranteed by a discrete Z_2 symmetry. The interactions between the dark matter and the SM fields are assumed to be induced by other heavy particles which decouple at the scale Λ . After writing down the subset of dim-6 operators (named dark operators) we are interested in,

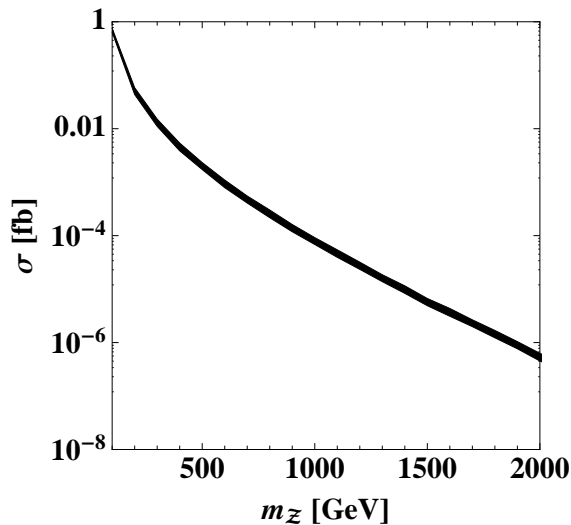


FIG. 22: Cross section of the vector DM \mathcal{Z} pair in the VBF process.

we examine the constraints on those dark operators from the relic abundance measurements and direct/indirect searches. The discovery potential for those dark operators at the LHC is also studied.

The dark matter candidate can be a scalar φ , a fermion χ or a vector \mathcal{Z} . We found that the fermion DM annihilation can be described by three independent operators ($\mathcal{O}_{f\chi}^L$, $\mathcal{O}_{f\chi}^R$, $\mathcal{O}_{\phi\chi}$), the scalar DM annihilation by four independent operators ($\mathcal{O}_{\phi 1}$, $\mathcal{O}_{\phi 2}$, $\mathcal{O}_{\phi 3}$, $\mathcal{O}_{f\phi}$) and the vector DM annihilation by one operator $\mathcal{O}_{\phi\mathcal{Z}}$. Owing to the different setups of various experiments, we can probe those dark operators separately.

Fermion DM χ : A positive signal at the CDMS II in the near future will indicate that the dark matter lie between [1000, 2000] TeV for the operators $\alpha_{f\chi}^{L/R}$ while [900, 1700] GeV for the operator $\alpha_{\phi\chi}$. Each individual fermion DM operator could satisfy the cosmic gamma-ray spectrum observed by the Fermi LAT since the contribution from the dark matter is far below the data. The allowed boost factors can be derived Galactic background agrees with the Fermi LAT measurement. For $m_\chi = 30 \text{ GeV} \sim 1000 \text{ GeV}$ the allowed boost factor $B = 20 \sim 600$. It is possible to detect the heavy dark matter signal from cosmic gamma-ray in the higher energy region due to the fact that the dark matter annihilation (including a boost factor) produces much more gamma-ray than the background, which is also true in the cases of scalar dark matter and vector dark matter discussed below. Furthermore, the fermion DM operator might be probed at the LHC via the mono-photon plus missing energy and mono-jet plus missing energy signatures.

Scalar DM φ : The family universal operators are almost ruled out by the CDMS II exclusion limit, while the family dependent operators is still allowed with a light scalar dark matter. The allowed boost factor is about $25 \sim 300$ for the scalar dark matter $m_\varphi = 45 \text{ GeV} \sim 800 \text{ GeV}$, if only $\alpha_{f\varphi}$ is non-zero. For non-vanishing $\alpha_{\phi 1}$ and non-vanishing $\alpha_{\phi 2}$ (or $\alpha_{\phi 3} = 1$, or $\alpha_{\phi 1} = \alpha_{\phi 2} = \alpha_{\phi 3} = \alpha_{f\phi} = 1$), the constraints are weaker, i.e. the allowed boost factor can be much larger. It is very challenging to search for such scalar dark matter at the LHC.

Vector DM \mathcal{Z} : There is no constraint from the CDMS II on vector DM operator as the scattering is mediated by the SM Higgs boson which is very small. The allowed boost factor is $120 \sim 2000$ for the dark matter $m_\varphi = 100 \text{ GeV} \sim 1000 \text{ GeV}$. The cross section of vector dark matter signal is too small to be detected at the LHC.

TABLE IV: Constraints and potential reaches of the dark operators of fermion and vector dark matter in various experiments. Shorthand notations: CII= CDMS II ; CIIp = projected CDMS II; SC(A/C)=SuperCDMS(Stage-A/C); B : boost factor need to fit Fermi LAT; ($\sqrt{\sqrt{}}$): full sensitivity; ($\sqrt{}$): good sensitivity; ($-$): not applicable or too small; (\times): no constraint; ($\times\times$): ruled out. DM mass and scale Λ are in the unit of GeV.

		$\Omega_{CDM}h^2$	direct search				Fermi	LHC (fb)		
		constraint	CII	CIIp	SC(A)	SC(C)	γ -ray	$\gamma + \cancel{E}_T$	$j + \cancel{E}_T$	VBF
χ	$\alpha_{f\chi}^L$	$m_\chi \sim [100, 2000]$ $\Lambda \sim [1000, 4000]$	$m_\chi > 1000$	$m_\chi < 1700$	$\sqrt{}$	$\sqrt{}$	$\sqrt{\sqrt{}}$: $m_\chi \sim 30, B \sim 20$ $\sqrt{}$: $m_\chi > 100$	$\sigma \sim [20, 1]$ for $m_\chi \sim [100, 400]$		—
	$\alpha_{f\chi}^R$	$m_\chi \sim [100, 2000]$ $\Lambda \sim [1000, 4000]$	$m_\chi > 1100$	$m_\chi < 1800$	$\sqrt{}$	$\sqrt{}$	$\sqrt{\sqrt{}}$: $m_\chi \sim 30, B \sim 20$ $\sqrt{}$: $m_\chi > 100$	$\sigma \sim [20, 1]$ for $m_\chi \sim [100, 400]$		—
	$\alpha_{\phi\chi}$	$m_\chi \sim [100, 2000]$ $\Lambda \sim [400, 2000]$	$m_\chi > 850$	$m_\chi < 1400$	$\sqrt{}$	$\sqrt{}$	$\sqrt{\sqrt{}}$: $m_\chi \sim 30, B \sim 20$ $\sqrt{}$: $m_\chi > 100$	—	—	—
	all	$m_\chi \sim [100, 2000]$ $\Lambda \sim [1000, 5500]$	$m_\chi > 250$	$m_\chi < 400$	$m_\chi < 1000$	$\sqrt{}$	$\sqrt{\sqrt{}}$: $m_\chi \sim 30, B \sim 20$ $\sqrt{}$: $m_\chi > 100$	$\sigma \sim [20, 0.001]$ for $m_\chi \sim [100, 20000]$		—
	\mathcal{Z}	$\alpha_{\phi\mathcal{Z}}$ $m_\chi \sim [100, 2000]$ $\Lambda \sim [600, 3000]$	\times	\times	\times	$\sqrt{}$ $m_h \sim 120$	$\sqrt{}$ large B	—	—	—

TABLE V: Constraints and potential reaches of the dark operators of scalar dark matter in various experiments. Shorthand notations: CII=CDMS II ; CIIp = projected CDMS II; SC(A/C)=SuperCDMS(Stage-A/C); B : boost factor need to fit Fermi LAT; ($\sqrt{\sqrt{}}$): full sensitivity; ($\sqrt{}$): good sensitivity; (-): not applicable or too small; (\times): no constraint; ($\times\times$): ruled out. DM mass and scale Λ are in the unit of GeV.

		$\Omega_{CDM}h^2$	direct search				Fermi	LHC (fb)		
		constraint	CII	CIIp	SC(A)	SC(C)	γ -ray	$\gamma + \cancel{E}_T$	$j + \cancel{E}_T$	VBF
φ [scenario A]	$\alpha_{f\phi}$	$m_\chi \sim [100, 2000]$ $\Lambda \sim 2000$	$\times\times$	$\times\times$	$\times\times$	$\times\times$	$\times\times$	$\times\times$	$\times\times$	$\times\times$
	$\alpha_{\phi 1}$	$m_\chi \sim [100, 500]$ $\Lambda \sim [1500, 500]$	$\times\times$	$\times\times$	$\times\times$	$\times\times$	$\times\times$	$\times\times$	$\times\times$	$\times\times$
	$\alpha_{\phi 2}$	$m_\chi \sim [100, 2000]$ $\Lambda \sim [600, 3500]$	$\times\times$	$\times\times$	$\times\times$	$\times\times$	$\times\times$	$\times\times$	$\times\times$	$\times\times$
	$\alpha_{\phi 3}$	$m_\chi \sim [100, 2000]$ $\Lambda \sim [600, 3400]$	$\times\times$	$\times\times$	$\times\times$	$\times\times$	$\times\times$	$\times\times$	$\times\times$	$\times\times$
	all	$m_\chi \sim [100, 2000]$ $\Lambda \sim [2000, 4500]$	$m_\varphi > 1500$ $m_\varphi < 2000$		$\sqrt{\sqrt{}}$	$\sqrt{\sqrt{}}$	$\sqrt{}$ large B			
	$\alpha_{f\phi}$	$m_\chi \sim [100, 2000]$ $\Lambda \sim [400, 1000]$	$m_\varphi > 100$ $m_\varphi < 150$ $m_\varphi \rightarrow 200$ $m_\varphi \rightarrow 300$				$\sqrt{}$ large $B \sim 100$	-	-	-
	$\alpha_{\phi 1}$	$m_\chi \sim [100, 500]$ $\Lambda \sim [1400, 500]$	-	-	-	$\sqrt{}$	$\sqrt{}$ huge $B > 1000$	-	-	-
φ [scenario B]	$\alpha_{\phi 2}$	$m_\chi \sim [100, 2000]$ $\Lambda \sim [600, 3600]$	-	-	-	-	$\sqrt{}$ huge $B > 1000$	-	-	-
	$\alpha_{\phi 3}$	$m_\chi \sim [100, 2000]$ $\Lambda \sim [400, 3000]$	-	-	-	-	$\sqrt{}$ huge $B > 1000$	-	-	-
	all	$m_\chi \sim [100, 2000]$ $\Lambda \sim [1400, 4500]$	$m_\varphi > 100$ $m_\varphi < 150$ $m_\varphi \rightarrow 200$ $m_\varphi \rightarrow 300$				$\sqrt{}$ large $B > 100$	-	-	-

Acknowledgments

We thank J. L. Rosner, Tim Tait, Jose Wudka and C.-P. Yuan for useful discussions. Q.-H. C. is supported by the Argonne National Laboratory and University of Chicago Joint Theory Institute (JTI) Grant 03921-07-137, and by the U.S. Department of Energy under Grants No. DE-AC02-06CH11357 and No. DE-FG02-90ER40560. C. R. C. is supported by the World Premier International Research Center Initiative (WPI initiative) by MEXT, Japan. C. S. Li is supported by the National Natural Science Foundation of China, under Grants No.10721063, No.10975004 and No.10635030. H. Z. is supported in part by the National Natural Science Foundation of China under Grants 10975004 and the China Scholarship Council (CSC) File No. 2009601282, and U. S. Department of Energy under Grants No. DE-AC02-06CH11357. C. R. C. thanks Institute of Physics, Academia Sinica in Taiwan for its hospitality during the final stages of this work.

Appendix A: Relic abundance

In the computation of the DM (χ) relic density, one assumes that χ was in thermal equilibrium with the SM particles in the early universe and decouple when it was non-relativistic. Once $\Gamma = n_\chi \langle \sigma^{ann} v \rangle < H$ ($H = (8\pi\rho/3M_{Pl})^{1/2}$ is the Hubble expansion rate), χ stopped annihilating and fell out of equilibrium, and its density remains intact till now. The number density n_χ is governed by the Boltzmann equation and the law of entropy conservation:

$$\frac{d}{dt}n_\chi = -3Hn_\chi - \langle \sigma v \rangle_{SA} (n_\chi^2 - n_{\chi,eq}^2) - \langle \sigma v \rangle_{CA} (n_\chi n_\phi - n_{\chi,eq} n_{\phi,eq}) + C_\Gamma, \quad (\text{A1})$$

$$\frac{ds}{dt} = -3Hs \quad (\text{A2})$$

where $\langle \sigma v \rangle$ is the thermally averaged annihilation cross section times the relative velocity, the subscripts SA and CA on $\langle \sigma v \rangle$ denote self-annihilation and co-annihilation (annihilation with another species ϕ) respectively, $n_{\chi,eq}$ denotes the equilibrium number density, and C_Γ is the contribution due to the decay of heavier particles into χ . Finally, s is the entropy density. For a massive cold dark matter candidate, its equilibrium density is given by the non-relativistic limit:

$$n_{\chi,eq} = g_\chi \left(\frac{mT}{2\pi} \right)^{3/2} e^{-m/T}, \quad (\text{A3})$$

where m is the mass of the particle species in question. The physics of Eq. (A1) is as following: At early times, when the temperature was higher than the mass of the particle, the number density was $n_{eq} \propto T^3$, χ annihilated with its own or other particle species ϕ into lighter states and vice versa. As the temperature decreased below the mass, n_χ dropped exponentially as indicated in Eq. (A3) and the annihilation rate $\Gamma = n \langle \sigma v \rangle$ dropped below H . The χ can no longer annihilate and its density per co-moving volume remains fixed. The temperature at which the particle decouples from the thermal bath is denoted T_F (freeze-out temperature) and roughly corresponds to the time when Γ is of the same order as H .

It is usually useful to scale out the effects of the expansion of the universe by considering the evolution of the number of particles in a co-moving volume. This is done by using the entropy density, s , as a fiducial quantity, and by defining as the dependent variable, $Y = n/s$ with $Y_{eq} = n_{\chi,eq}/s$. In this case, Eq. (A1) can be rewritten as

$$\frac{dY}{dx} = \frac{1}{3H} \frac{ds}{dx} \langle \sigma v \rangle_{SA} (Y_\chi^2 - Y_{\chi,eq}^2) + \frac{1}{3H} \frac{ds}{dx} \langle \sigma v \rangle_{CA} (Y_\chi Y_\phi - Y_{\chi,eq} Y_{\phi,eq}), \quad (\text{A4})$$

where $x = m/T$. In radiation domination era, the entropy, as function of the temperature, is given by

$$s = \frac{2\pi^2}{45} g_{*s}(x) \left(\frac{m}{x}\right)^3 \equiv k_1 x^{-3},$$

which is deduced from the fact that $s = (\rho + P)/T$ and g_{*s} is the effective degrees of freedom for the entropy density. Therefore, one finds

$$\frac{ds}{dx} = -\frac{3s}{x}. \quad (\text{A5})$$

Hence, the Boltzmann equation for the DM number density is obtained

$$\frac{dY}{dx} = -\frac{s}{Hx} \left\{ \langle \sigma v \rangle_{SA} (Y_\chi^2 - Y_{\chi,eq}^2) \right\}. \quad (\text{A6})$$

As is well known, $\langle \sigma v \rangle$ is well approximated by a non-relativistic expansion (obtained by replacing the square of the energy in the center of mass frame by $s = 4m^2 + m^2 v^2$):

$$\langle \sigma v \rangle = a + b \langle v^2 \rangle + \mathcal{O}(\langle v^4 \rangle) \approx a + 6\frac{b}{x}. \quad (\text{A7})$$

The freeze-out temperature is defined by solving the following equation

$$x_F = \ln \left(c(c+2) \sqrt{\frac{45}{8}} \frac{g}{2\pi^3} \frac{m M_{Pl} (a + 6b/x_F)}{g_*^{1/2} x_F^{1/2}} \right), \quad (\text{A8})$$

where c is a constant of order one determined by matching the later-time and early-time solutions. The result does not depend dramatically on the precise value of c which we will choose the usual value $c = 1/2$.

Appendix B: Dark matter annihilation

1. Fermionic dark matter annihilation

The relevant cross sections for pair of χ to annihilate have final states into fermions, into Higgs bosons, or into pair of Higgs boson and Z -boson. The Feynman diagrams of the annihilations are shown in Fig. 2. Summing/averaging over final/initial spins and integrating over the phase space of the final state particles, we obtain the cross sections of $\chi\bar{\chi}$ annihilation shown below.

a. $\chi\bar{\chi} \rightarrow f\bar{f}$

The annihilation cross section into a fermion pair is given by

$$\begin{aligned} & \sigma(\chi\bar{\chi} \rightarrow f\bar{f}) \\ &= \frac{N_C \beta_f}{12\pi s \beta \Lambda^4} \left\{ (g_L^2 + g_R^2) [s^2 - s(m^2 + m_f^2) + 4m^2 m_f^2] + 6g_L g_R (s - 2m^2) m_f^2 \right\}, \end{aligned} \quad (\text{B1})$$

where $\beta \equiv \sqrt{1 - 4m^2/s}$, $\beta_f \equiv \sqrt{1 - 4m_f^2/s}$ and the factor N_C sums over the different color combinations allowed in the final state, $N_C = 3$ for quarks and $N_C = 1$ for leptons. The couplings g_L and g_R are given in Eq. 7. Expanding σv_{rel} in powers of the relative speed between the χ fermions, v_{rel} , gives

$$a = N_C \frac{m^2}{2\pi \Lambda^4} \sqrt{1 - r_f^2} (g_L^2 + g_R^2 + r_f^2 g_L g_R), \quad (\text{B2})$$

$$b = N_C \frac{m^2}{48\pi \Lambda^4 \sqrt{1 - r_f^2}} \left\{ (g_L^2 + g_R^2) (2r_f^4 - 10r_f^2 + 11) + 3g_L g_R r_f^2 (3 - 2r_f^2) \right\}, \quad (\text{B3})$$

where $r_f \equiv m_f/m$.

b. $\chi\bar{\chi} \rightarrow Z \rightarrow f\bar{f}$

The annihilation cross section into a fermion pair via the Z -mediated s -channel process is given by

$$\sigma(\chi\bar{\chi} \rightarrow Z \rightarrow f\bar{f}) = N_C \frac{\alpha_{\phi\chi}^2}{48\pi\beta\Lambda^4} (g_{ZL}^2 + g_{ZR}^2) \frac{v^2 (s - m^2) m_Z^2}{(s - m_Z^2)^2 + m_Z^2 \Gamma_Z^2}, \quad (\text{B4})$$

where $g_{ZL/R}$ denotes the SM couplings of the Z -boson to fermions and $m_Z (\Gamma_Z)$ denotes the mass (width) of the Z -boson. We have ignored the masses of the SM fermions in the annihilation cross section of the $\chi\bar{\chi} \rightarrow Z \rightarrow f\bar{f}$ process because it only contributes around the Z -pole region, i.e. $m_{DM} \approx \frac{1}{2}m_Z$, where the masses of the SM lepton and light quarks are negligible. The corresponding leading terms in the non-relativistic expansion are

$$a = N_C \frac{\alpha_{\phi\chi}^2 m^2}{8\pi \Lambda^4} (g_{ZL}^2 + g_{ZR}^2) \frac{m_Z^2 v^2}{(4m^2 - m_Z^2)^2 + m_Z^2 \Gamma_Z^2}, \quad (\text{B5})$$

$$b = -N_C \frac{\alpha_{\phi\chi}^2 m^2}{192\pi \Lambda^4} (g_{ZL}^2 + g_{ZR}^2) \frac{16m^4 + 40m_Z^2 m^2 - 11m_Z^4}{(4m^2 - m_Z^2)^2 + m_Z^2 \Gamma_Z^2}. \quad (\text{B6})$$

As to be shown later, this annihilation channel is dominant around the Z -pole region, i.e. $m \sim \frac{1}{2}m_Z$, but its contribution decreases so rapidly, once m_χ goes beyond the Z -pole, that it is overwhelmed by other annihilation channels.

c. $\chi\bar{\chi} \rightarrow hZ$

The annihilation cross section into a pair of Z -boson and Higgs scalar shown in Fig. 2(c) is given by

$$\begin{aligned} & \sigma(\chi\bar{\chi} \rightarrow hZ) \\ &= \frac{\alpha_{\phi\chi}^2}{96\pi s^3 \beta \Lambda^4} \sqrt{\lambda(s, m_Z^2, m_h^2)} \left\{ (s + 2m^2) \lambda(s, m_Z^2, m_h^2) + 12s m_Z^2 (3m^2 - s) \right\}, \quad (\text{B7}) \end{aligned}$$

where the function λ being defined as

$$\lambda(x, y, z) = (x - y - z)^2 - 4yz.$$

The non-relativistic expansion gives rise to the following leading terms

$$\begin{aligned} a &= \frac{\alpha_{\phi\chi}^2 m^2}{512\pi\Lambda^4} \lambda^{1/2}(4, r_h^2, r_Z^2) [\lambda(4, r_h^2, r_Z^2) - 8r_Z^2] \\ b &= \frac{\alpha_{\phi\chi}^2 m^2}{12288\pi\Lambda^4} \lambda^{-1/2}(4, r_h^2, r_Z^2) \left[1792 - 128(5r_h^2 + 26r_Z^2) \right. \\ &\quad \left. - 64(3r_h^4 - 16r_h^2 r_Z^2 - 16r_Z^4) + 8(13r_h^2 - 2r_Z^2)(r_h^2 - r_Z^2) - 11(r_h^2 - r_Z^2)^4 \right]. \quad (\text{B9}) \end{aligned}$$

where $r_{h(Z)} \equiv m_{h(Z)}/m$.

d. $\chi\bar{\chi} \rightarrow Z \rightarrow hZ$

The annihilation into a pair of Z -boson and Higgs scalar can also be induced by the Z -mediated s -channel process, see Fig. 2(d). This annihilation channel opens only if $2m > m_Z + m_h$, which implies $s \approx 4m^2 > 4m_Z^2$, thus its contribution is highly suppressed so that we can ignore it in this study.

e. $\chi\bar{\chi} \rightarrow Z \rightarrow W^+W^-$

For this channel,

$$a = \frac{\alpha_{\phi\chi}^2 m^2}{16\pi\Lambda^4} (1 - r_W^2)^{1/2} \left(1 + 4r_W^2 - \frac{17}{4}r_W^4 - \frac{3}{4}r_W^6 \right) \left(1 - \frac{r_Z^2}{4} \right)^{-2}, \quad (\text{B10})$$

$$b = \frac{7\alpha_{\phi\chi}^2 m^2}{384\pi\Lambda^4} (1 - r_W^2)^{1/2} \left[1 + r_W^2 + \frac{145}{28}r_W^4 + \frac{3}{2}r_W^6 - \frac{r_Z^2}{28} \left(19 + 55r_W^2 - \frac{59}{4}r_W^4 + 6r_W^6 \right) \right] \left(1 - \frac{r_Z^2}{4} \right)^{-3}, \quad (\text{B11})$$

where $r_{W(Z)} = m_{W(Z)}/m$.

2. Scalar dark matter annihilation

When the scalar φ is the DM, we must consider a large number of annihilation processes, e.g. $\varphi\varphi \rightarrow f\bar{f}/WW/ZZ/hh$ and $\varphi\varphi \rightarrow h \rightarrow f\bar{f}/WW/ZZ/hh$, see Fig. 10. The latter, Higgs-mediated s -channel processes, contributes significantly around the Higgs resonance region only.

a. $\varphi\varphi \rightarrow f\bar{f}$

In the scenario-A, the annihilation cross sections of $\varphi\varphi \rightarrow f\bar{f}$ read as

$$\sigma(\varphi\varphi \rightarrow f\bar{f}) = N_C \frac{\alpha_{f\phi}^2 v^2}{16\pi\beta\Lambda^4} \beta_f^{3/2} + N_C \frac{\alpha_{\phi 1}^2 v^2}{32\pi\beta\Lambda^4} \beta_f^{3/2} \frac{v^2 m_f^2}{(s - m_h^2)^2 + m_h^2 \Gamma_h^2}, \quad (\text{B12})$$

where the first and second term corresponds to Fig. 10(a) and (b), respectively. Expanding σv_{rel} in powers of the relative speed v_{rel} gives the following leading terms

$$a = N_C \frac{v^2}{16\pi\Lambda^4} (1 - r_f^2)^{3/2} \left[2\alpha_{f\phi}^2 + \alpha_{\phi 1}^2 \frac{m_f^2 v^2}{(4m^2 - m_h^2)^2 + m_h^2 \Gamma_h^2} \right], \quad (\text{B13})$$

$$b = N_C \frac{v^2}{128\pi\Lambda^4} \sqrt{1 - r_f^2} \left\{ 2\alpha_{f\phi}^2 (2r_f^2 + 1) + \alpha_{\phi 1}^2 r_f^2 \frac{v^2 [-48m^6 + 8(12m_f^2 + m_h^2)m^4 + m_h^2(m_h^2 - 32m_f^2)m^2 + 2m_f^2 m_h^4]}{((4m^2 - m_h^2)^2 + m_h^2 \Gamma_h^2)^2} \right\} \quad (\text{B14})$$

Similarly, in the scenario-B, the leading terms are given by

$$a = N_C \frac{v^2}{16\pi\Lambda^4} (1 - r_f^2)^{3/2} \left[2\alpha_{f\phi}^2 \left(\frac{m_f^2}{v^2} \right) + \alpha_{\phi 1}^2 \frac{m_f^2 v^2}{(4m^2 - m_h^2)^2 + m_h^2 \Gamma_h^2} \right], \quad (\text{B15})$$

$$b = N_C \frac{v^2}{128\pi\Lambda^4} \sqrt{1 - r_f^2} \left\{ 2\alpha_{f\phi}^2 (2r_f^2 + 1) \left(\frac{m_f^2}{v^2} \right) + \alpha_{\phi 1}^2 r_f^2 \frac{v^2 [-48m^6 + 8(12m_f^2 + m_h^2)m^4 + m_h^2(m_h^2 - 32m_f^2)m^2 + 2m_f^2 m_h^4]}{\left((4m^2 - m_h^2)^2 + m_h^2 \Gamma_h^2 \right)^2} \right\} \quad (\text{B16})$$

b. $\varphi\varphi \rightarrow WW/ZZ$

The annihilation cross sections of $\varphi\varphi$ annihilation into vector bosons are given by

$$\sigma(\varphi\varphi \rightarrow VV) = \delta_V \frac{\beta_V (s^2 - 4s m_V^2 + 12m_V^4)}{64\pi s \beta \Lambda^4} \left(\alpha_{\phi 3}^2 + \frac{\alpha_{\phi 1}^2 v^4}{(s - m_h^2)^2 + m_h^2 \Gamma_h^2} \right) \quad (\text{B17})$$

where the subscript V denotes the type of vector boson and $\beta_V = \sqrt{1 - 4m_V^2/s}$. δ_V counts for the identical particle: $\delta_W = 1$ and $\delta_Z = 1/2$. The first and second term in Eq. B17 corresponds to Fig. 10(c) and (d), respectively. The non-relativistic expansion gives rise to the following leading terms

$$a_V = \frac{\delta_V}{32\pi m^3 \Lambda^4} \sqrt{m^2 - m_V^2} \times \left\{ \alpha_{\phi 3}^2 (4m^4 - 4m_V^2 m^2 + 3m_V^4) + \alpha_{\phi 1}^2 v^4 \frac{4m^4 - 4m_V^2 m^2 + 3m_V^4}{(m_h^2 - 4m^2)^2 + m_h^2 \Gamma_h^2} \right\}, \quad (\text{B18})$$

$$b_V = \frac{\delta_V}{256\pi m^3 \Lambda^4} \frac{1}{\sqrt{m^2 - m_V^2}} \times \left\{ 3\alpha_{\phi 3}^2 (4m^6 - 4m_V^2 m^4 - m_V^4 m^2 + 2m_V^6) + \frac{\alpha_{\phi 1}^2 v^4 (4m^2 - m_h^2)}{\left((m_h^2 - 4m^2)^2 + m_h^2 \Gamma_h^2 \right)^2} \left[16m^8 + 4(3m_h^2 - 20m_V^2)m^6 - 4(3m_h^2 m_V^2 - 31m_V^4)m^4 + 3m_V^4(m_h^2 + 24m_V^2)m^2 + 6m_h^2 m_V^6 \right] \right\}. \quad (\text{B19})$$

c. $\varphi\varphi \rightarrow hh$

The cross section of $\varphi\varphi \rightarrow hh$ reads as

$$\sigma(\varphi\varphi \rightarrow hh) = \frac{\beta_h (c_1 v^2 + c_2 s)^2}{32\pi s \beta \Lambda^4} + \frac{9v^4 \alpha_{\phi 1}^2}{128\pi s \beta \Lambda^4} \frac{\beta_h m_h^4}{(s - m_h^2)^2 + m_h^2 \Gamma_h^2}, \quad (\text{B20})$$

where

$$c_1 = \frac{3}{4} \alpha_{\phi 1}, \quad c_2 = \alpha_{\phi 2} + \frac{\alpha_{\phi 3}}{4}.$$

The first and second term in Eq. B20 corresponds to Fig. 10(e) and (f), respectively. The non-relativistic expansion gives the following leading terms

$$a = \frac{\sqrt{m^2 - m_h^2}}{128\pi m^3 \Lambda^4} \left[2(c_1 v^2 + 4c_2 m^2)^2 + \frac{9\alpha_{\phi 1}^2 m_h^4 v^4}{(4m^2 - m_h^2)^2 + m_h^2 \Gamma_h^2} \right], \quad (\text{B21})$$

$$b = \frac{(4c_2 m^2 + c_1 v^2) [4c_2 m^2 (3m^2 - 2m_h^2) - c_1 v^2 (m^2 - 2m_h^2)]}{512\pi m^3 \Lambda^4 \sqrt{m^2 - m_h^2}} + \frac{9\alpha_{\phi 1}^2 m_h^4 (-80m^6 + 120m_h^2 m^4 - 33m_h^4 m^2 + 2m_h^6) v^4}{2048\pi m^3 \Lambda^4 \sqrt{m^2 - m_h^2} [(m_h^2 - 4m^2)^2 + m_h^2 \Gamma_h^2]^2}. \quad (\text{B22})$$

3. Vector dark matter annihilation

The vector DM \mathcal{Z} can either directly annihilate into the Higgs boson pair or annihilate into the fermion, Higgs scalar and vector boson pair through the Higgs-mediated s -channel process, see Fig. 17

a. $\mathcal{Z}\mathcal{Z} \rightarrow hh$

The annihilation cross section of $\mathcal{Z}\mathcal{Z} \rightarrow hh$ is given by

$$\sigma(\mathcal{Z}\mathcal{Z} \rightarrow hh) = \frac{\alpha_{\phi \mathcal{Z}}^2 \beta_h (6m^4 - 4s m^2 + s^2)}{256s \beta \Lambda^4}, \quad (\text{B23})$$

which gives rise to the leading term in the non-relativistic expansion as follows:

$$a = \frac{3\alpha_{\phi \mathcal{Z}}^2 m^2}{256\pi \Lambda^4} \sqrt{1 - r_h^2}, \quad b = \frac{\alpha_{\phi \mathcal{Z}}^2 (13m^2 - 10m_h^2)}{2048\pi \Lambda^4 \sqrt{1 - r_h^2}}. \quad (\text{B24})$$

b. $\mathcal{Z}\mathcal{Z} \rightarrow h \rightarrow hh$

The annihilation cross section of $\mathcal{Z}\mathcal{Z}$ pair into the Higgs scalar pair via the Higgs-mediated s -channel process is given by

$$\sigma(\mathcal{Z}\mathcal{Z} \rightarrow h \rightarrow hh) = \frac{9\alpha_{\phi\mathcal{Z}}^2 \beta_h m_h^4 (6m^4 - 4s m^2 + s^2)}{64\pi s \beta \Lambda^4 (s - m_h^2)^2 + m_h^2 \Gamma_h^2}, \quad (\text{B25})$$

which yields the following leading non-relativistic expansion terms

$$a = \frac{27\alpha_{\phi\mathcal{Z}}^2}{64\pi\Lambda^4} \frac{m^2 m_h^4 \sqrt{1 - r_h^2}}{(m_h^2 - 4m^2)^2 + m_h^2 \Gamma_h^2}, \quad (\text{B26})$$

$$b = \frac{9\alpha_{\phi\mathcal{Z}}^2}{512\pi\Lambda^4} \frac{(4m^2 - m_h^2)(4m^4 - 5m_h^2 m^2 + 10m_h^4)}{\sqrt{1 - r_h^2} \left((m_h^2 - 4m^2)^2 + m_h^2 \Gamma_h^2 \right)^2}. \quad (\text{B27})$$

c. $\mathcal{Z}\mathcal{Z} \rightarrow h \rightarrow f\bar{f}$

The annihilation cross section of $\mathcal{Z}\mathcal{Z} \rightarrow h \rightarrow f\bar{f}$ is given by

$$\sigma(\mathcal{Z}\mathcal{Z} \rightarrow h \rightarrow f\bar{f}) = N_C \frac{\alpha_{\phi\mathcal{Z}}^2 \beta_f^{3/2} m_f^2 (6m^4 - 4s m^2 + s^2)}{16\pi \beta \Lambda^4 (s - m_h^2)^2 + m_h^2 \Gamma_h^2}, \quad (\text{B28})$$

which yields

$$a = N_C \frac{3\alpha_{\phi\mathcal{Z}}^2 m_f^2}{4\pi\Lambda^4} \frac{m^4 (1 - r_f^2)^{3/2}}{(m_h^2 - 4m^2)^2 + m_h^2 \Gamma_h^2}, \quad (\text{B29})$$

$$b = N_C \frac{\alpha_{\phi\mathcal{Z}}^2 m_f^2}{32\pi\Lambda^4} \sqrt{1 - r_f^2} \frac{m^2 (4m^2 - m_h^2) (28m^4 + (8m_f^2 - 19m_h^2) m^2 + 10m_f^2 m_h^2)}{\left((m_h^2 - 4m^2)^2 + m_h^2 \Gamma_h^2 \right)^2}. \quad (\text{B30})$$

We note that both a and b are proportional to m_f so that they are negligible in the limit of $m \gg m_f$.

d. $\mathcal{Z}\mathcal{Z} \rightarrow h \rightarrow WW/ZZ$

The annihilation cross section of $\mathcal{Z}\mathcal{Z}$ into vector boson pair is given by

$$\sigma(\mathcal{Z}\mathcal{Z} \rightarrow h \rightarrow VV) = \delta_V \frac{\alpha_{\phi\mathcal{Z}}^2 \beta_V (6m^4 - 4s m^2 + s^2) (12m_V^2 - 4s m_V^2 + s^2)}{32\pi s \beta \Lambda^4 (s - m_h^2)^2 + m_h^2 \Gamma_h^2}, \quad (\text{B31})$$

where $\delta_W = 1$ and $\delta_Z = 1/2$. The non-relativistic expansion gives rise to the two leading terms as follows:

$$a_V = \delta_V \frac{3\alpha_{\phi Z}^2 m^2}{8\pi\Lambda^4} \sqrt{1 - r_V^2} \frac{4m^4 - 4m_V^2 m^2 + 3m_V^4}{(4m^2 - m_h^2)^2 + m_h^2 \Gamma_h^2}, \quad (\text{B32})$$

$$b_V = \delta_V \frac{\alpha_{\phi Z}^2}{64\pi\Lambda^4 \sqrt{1 - r_V^2}} \frac{(4m^2 - m_h^2)}{\left((4m^2 - m_h^2)^2 + m_h^2 \Gamma_h^2\right)^2} \left\{ 208m^8 - 4(25m_h^2 + 68m_V^2)m^6 \right. \\ \left. + 4(19m_V^4 + 41m_h^2 m_V^2)m^4 + (24m_V^6 - 103m_h^2 m_V^4)m^2 + 30m_h^2 m_V^6 \right\} \quad (\text{B33})$$

Appendix C: Dark matter direct detection

1. Fermionic DM-nucleon interaction

When the DM is a fermion χ , its coupling to quark, leading to elastics scattering from a nucleus, can be parametrized as Eq. 13, of which the first term results in a spin-independent scattering from a nucleus while the second term leads to a spin-dependent scattering from a nucleus.

Consider the SI scattering first. When a WIMP interact with quarks via a vector-like interaction, e.g. given by

$$\mathcal{L}_V = b_q \bar{\chi} \gamma_\mu \chi \bar{q} \gamma^\mu q, \quad (\text{C1})$$

where b_q is a shorthand notation of the WIMP-quark vector coupling given in the first term of Eq. 13. In this case, the contributions of each quark in the nucleus add coherently and large cross sections result for large nuclei. The WIMP-nucleus cross section in this case is

$$\sigma_{\chi N}^{SI} = \frac{m_{DM}^2 m_N^2 b_N^2}{\pi (m_{DM} + m_N)^2}, \quad (\text{C2})$$

where $b_N = 2Z b_p + (A - Z) b_n$ with $b_p = 2b_u + b_d$ and $b_n = b_u + 2b_d$. It is convenient to consider the cross section with the single nucleon for comparing with the experiment. Through a simple algebra calculation, we obtained the cross sections of WIMP-proton and

WIMP-neutron as given below:

$$\begin{aligned}\sigma_{\chi p}^{SI} &= \frac{m_{DM}^2 m_p^2}{\pi (m_{DM} + m_p)^2} \frac{1}{16\Lambda^4} \left[3 (\alpha_{q\chi}^R - \alpha_{q\chi}^L) + \alpha_{\phi\chi} \frac{g}{4 \cos \theta_W} \frac{v}{m_Z} (1 - 4s_W^2) \right]^2 \\ &\approx (6.98 \times 10^{-5} \text{ pb}) \left(\frac{\text{TeV}}{\Lambda} \right)^4 (\alpha_{q\chi}^R - \alpha_{q\chi}^L + 0.013\alpha_{\phi\chi})^2,\end{aligned}\quad (\text{C3})$$

$$\begin{aligned}\sigma_{\chi n}^{SI} &= \frac{m_{DM}^2 m_n^2}{\pi (m_{DM} + m_p)^2} \frac{1}{16\Lambda^4} \left[3 (\alpha_{q\chi}^R - \alpha_{q\chi}^L) - \alpha_{\phi\chi} \frac{g}{4 \cos \theta_W} \frac{v}{m_Z} \right]^2 \\ &\approx (6.98 \times 10^{-5} \text{ pb}) \left(\frac{\text{TeV}}{\Lambda} \right)^4 (\alpha_{q\chi}^R - \alpha_{q\chi}^L - 0.162\alpha_{\phi\chi})^2.\end{aligned}\quad (\text{C4})$$

Now consider the SD scattering. WIMPs could also couple to the spin of the target nucleus through an ‘‘axial-vector’’ interaction

$$\mathcal{L}_A = d_q \bar{\chi} \gamma_\mu \gamma_5 \chi \bar{q} \gamma^\mu \gamma_5 q, \quad (\text{C5})$$

where d_q is the shorthand notation of the axial coupling given in the second term of Eq. 13. The spin-dependent WIMP-nuclei elastic scattering cross section can be expressed as

$$\sigma_{\chi N}^{SD} \approx \frac{32m_{DM}^2 m_N^2}{\pi (m_{DM} + m_N)^2} [\Lambda_N^2 J(J+1)], \quad (\text{C6})$$

where J is the total angular momentum of the nucleus. $\Lambda_N (\propto 1/J)$ depends on the axial couplings of WIMPs to the quarks,

$$\Lambda_N \equiv \frac{a_p \langle S_p \rangle + a_n \langle S_n \rangle}{J}.$$

where

$$a_p = d_u \Delta_u^p + d_d \Delta_d^p + d_s \Delta_s^p, \quad a_n = d_u \Delta_u^n + d_d \Delta_d^n + d_s \Delta_s^n.$$

Here, Δ ’s are the fraction of the nucleon spin carried by a given quark. Their values are measured to be [78]

$$\Delta_u^p = \Delta_d^n = 0.78 \pm 0.02, \quad \Delta_d^p = \Delta_u^n = -0.48 \pm 0.02, \quad \Delta_s^p = \Delta_s^n = -0.15 \pm 0.02.$$

$\langle S_p \rangle$ and $\langle S_n \rangle$ are the expectation values of the total spin of protons and neutrons, respectively, whose values depend on the number of protons and neutrons in the nucleus being considered, namely, whether it is odd or even. For odd-proton nuclei the spin-dependent WIMP-nucleus cross section is mainly due to the WIMP-proton interactions, whereas for odd-neutron nuclei it is dominated by WIMP-neutron scattering. For even-even nuclei the

spin-dependent cross-section is highly suppressed. For a proton and a neutron as a target, Eq. 17 is transformed into the cross section form WIMP-proton (neutron) interactions with the proton (neutron) spins $\langle S_{p,n} \rangle = 1/2$ and $J = 1/2$. Thus, the SD cross section of WIMP-proton and WIMP-neutron are given by

$$\begin{aligned}\sigma_{\chi p}^{SD} &= \frac{24 m_D^2 m_p^2}{\pi (m_D + m_p)^2} \frac{1}{16\Lambda^4} [0.15\alpha_{q\chi}^R + 0.15\alpha_{q\chi}^L - 0.68\alpha_{\phi\chi}]^2 \\ &\approx (4.183 \times 10^{-6} \text{ pb}) \left(\frac{\text{TeV}}{\Lambda} \right)^4 (\alpha_{q\chi}^R + \alpha_{q\chi}^L - 4.53\alpha_{\phi\chi})^2, \\ \sigma_{\chi n}^{SD} &= \frac{24 m_D^2 m_n^2}{\pi (m_D + m_n)^2} \frac{1}{16\Lambda^4} [0.15\alpha_{q\chi}^R + 0.15\alpha_{q\chi}^L + 0.54\alpha_{\phi\chi}]^2 \\ &\approx (4.183 \times 10^{-6} \text{ pb}) \left(\frac{\text{TeV}}{\Lambda} \right)^4 (\alpha_{q\chi}^R + \alpha_{q\chi}^L + 3.53\alpha_{\phi\chi})^2.\end{aligned}$$

2. Scalar DM-nucleon interaction

When the DM is a scalar φ , it can be detected in the spin-independent experiments via the scalar interaction with nucleus

$$\mathcal{L}_{\varphi qq} = \frac{1}{\Lambda^2} \frac{\alpha_{f\phi} v}{\sqrt{2}} \varphi \bar{q} q + \frac{1}{\Lambda^2} \frac{\alpha_{\phi 1} v^2}{2} \frac{m_q}{m_h^2} \varphi \bar{q} q, \quad (\text{C7})$$

which leads to the scattering amplitude

$$\langle \mathcal{M} \rangle = \mathcal{C}_{\varphi q} \langle \bar{q} q \rangle,$$

where $\langle \rangle$ denotes an average and sum over the spins of the initial and final state quarks, respectively, and the coefficient $\mathcal{C}_{\varphi q}$ is given by

$$\mathcal{C}_{\varphi q} = \frac{1}{\Lambda^2} \left(\frac{\alpha_{f\phi} v}{\sqrt{2}} + \frac{\alpha_{\phi 1} v^2}{2} \frac{m_q}{m_h^2} \right).$$

The matrix element $\langle \bar{q} q \rangle$ of quarks in a nucleon state is given in [16] by

$$\langle \bar{q} q \rangle = \frac{m_{p,n}}{m_q} f_{Tq}^{(p,n)} \text{ (light quarks)}; \quad \langle \bar{q} q \rangle = \frac{2}{27} \frac{m_{p,n}}{m_q} f_{Tg}^{(p,n)} \text{ (heavy quarks)}.$$

Summing over quark flavors, we obtain the φ -nucleon couplings:

$$f_{\varphi q}^{(p,n)} = \sum_{q=u,d,s} f_{Tq}^{(p,n)} \mathcal{C}_{\varphi q} \frac{m_{p,n}}{m_q} + \frac{2}{27} f_{Tg}^{(p,n)} \sum_{q=c,b,t} \mathcal{C}_{\varphi q} \frac{m_{p,n}}{m_q}, \quad (\text{C8})$$

where [79, 80]

$$\begin{aligned} f_{T_u}^{(p)} &\approx 0.020 \pm 0.004, & f_{T_d}^{(p)} &\approx 0.026 \pm 0.005, & f_{T_s}^{(p)} &\approx 0.118 \pm 0.062, \\ f_{T_u}^{(n)} &\approx 0.014 \pm 0.003, & f_{T_d}^{(n)} &\approx 0.036 \pm 0.008, & f_{T_s}^{(n)} &\approx 0.118 \pm 0.062. \end{aligned} \quad (\text{C9})$$

The first term in Eq. C8 corresponds to interaction with the quarks in the target nuclei, while the second term corresponds to interactions with the gluons in the target through a quark loop diagram. $f_{T_g}^{(p)}$ is given by $1 - f_{T_u}^{(p)} - f_{T_d}^{(p)} - f_{T_s}^{(p)} \approx 0.84$, and analogously, $f_{T_g}^{(n)} \approx 0.83$. Note that we have to sum over the couplings to each nucleon before squaring because the wavelength associated with the momentum transfer is comparable to or larger than the size of nucleus, the so-called ‘‘coherence effect’’. Due to such a coherence effect with the entire nucleus, the cross section for spin-independent interactions scales approximately as the square of the atomic mass of the target nucleus [81].

The total spin-independent WIMP-nuclei cross section at zero momentum transfer is given by

$$\sigma_{\varphi N}^{SI} = \frac{m_N^2}{4\pi (m_{DM} + m_N)^2} [Z f_{\varphi q}^{(p)} + (A - Z) f_{\varphi q}^{(n)}]^2, \quad (\text{C10})$$

where m_N is the target nuclei’s mass, and Z and A are the atomic number and atomic mass of the nucleus. In order to compare with the experimental sensitivities and limits which are often described in terms of the dark matter elastic scattering with nucleons, we derive the φ -nucleon cross section as following:

$$\sigma_{\varphi p}^{SI} = \frac{m_p^2}{4\pi (m_{DM} + m_p)^2} [f_{\varphi p}^{(p)}]^2, \quad \sigma_{\varphi n}^{SI} = \frac{m_n^2}{4\pi (m_{DM} + m_n)^2} [f_{\varphi n}^{(n)}]^2.$$

In practices, we found $\sigma_{\varphi p}^{SI} \simeq \sigma_{\varphi n}^{SI}$.

3. Vector DM-nucleon interaction

Since the vector DM \mathcal{Z} only talks to the Higgs boson in our model, it can be detected in the spin-independent experiments. The relevant Lagrangian is given by

$$\mathcal{L}_{\mathcal{Z}Zqq} = \frac{\alpha_{\phi\mathcal{Z}}}{2\Lambda^2} \frac{m_q}{m_h^2} C_{\mu\nu} C^{\mu\nu} \bar{q}q,$$

which gives rise to the following scattering amplitude

$$i\mathcal{M}_{\mathcal{Z}Zqq} = \frac{\alpha_{\phi\mathcal{Z}}}{\Lambda^2} \frac{m_q}{m_h^2} [(p_1 \cdot p_3) g^{\mu\nu} - p_1^\nu p_3^\mu] \varepsilon_\nu^*(p_3) \varepsilon_\mu(p_1) \bar{q}(p_4) q(p_2).$$

In the extreme non-relativistic limit, $p_1 = p_3 = (m_{DM}, 0)$ and the polarization vector of the heavy vector \mathcal{Z} are purely spatial, $\varepsilon^\mu(p_{1,3}) = (0, \vec{\varepsilon}_{1,3})$. The above amplitude is thus simplified as

$$i\mathcal{M}_{\mathcal{Z}\mathcal{Z}q\bar{q}} = \mathcal{C}_{\mathcal{Z}q} \varepsilon_\mu^*(p_3) \varepsilon^\mu(p_1) \bar{q}(p_4) q(p_2),$$

where

$$\mathcal{C}_{\mathcal{Z}q} = \alpha_{\phi\mathcal{Z}} \frac{m_D^2}{\Lambda^2} \frac{m_q}{m_h^2}.$$

The effective WIMP-nucleon scattering cross section is thus given by

$$\sigma_{\mathcal{Z}p, \mathcal{Z}n}^{SI} = \frac{m_{p,n}^2}{4\pi (m_D + m_{p,n})^2} \left[Z f_{\mathcal{Z}q}^{(p,n)} + (A - Z) f_{\mathcal{Z}q}^{(p,n)} \right]^2,$$

where the \mathcal{Z} -nucleon couplings, $f_{\mathcal{Z}q}^{(p,n)}$, are given by

$$f_{\mathcal{Z}q}^{(p,n)} = \sum_{q=u,d,s} f_{T_q}^{(p,n)} \mathcal{C}_{\mathcal{Z}q} \frac{m_{p,n}}{m_q} + \frac{2}{27} f_{T_G}^{(p,n)} \sum_{q=c,b,t} \mathcal{C}_{\mathcal{Z}q} \frac{m_{p,n}}{m_q}.$$

Again, using $m_p \simeq m_n$ and $m_D \gg m_{p,n}$, we obtain the effective WIMP-nucleon cross section, $\sigma_{\mathcal{Z}p}^{SI} (= \sigma_{\mathcal{Z}n}^{SI})$ as following:

$$\begin{aligned} \sigma_{\mathcal{Z}p}^{SI} &= \frac{\alpha_{\phi\mathcal{Z}}^2}{4\pi} \left(\frac{m_D^2}{\Lambda^4} \right) \left(\frac{m_p}{m_h} \right)^4 \left[f_{T_s} + \frac{6}{27} f_{T_G} \right]^2. \\ &\approx (2.88 \times 10^{-10} \text{ pb}) \alpha_{\phi\mathcal{Z}}^2 \left(\frac{m_D}{100 \text{ GeV}} \right)^2 \left(\frac{\text{TeV}}{\Lambda} \right)^4 \left(\frac{100 \text{ GeV}}{m_h} \right)^4 \end{aligned}$$

The SI elastic \mathcal{Z} -nucleon scattering cross sections are plotted in Fig. 19, along with the projected future sensitivity of SuperCDMS, Stage-A (blue dashed line) and Stage-C (black dashed curve). The cross sections are well below all the current bound from CDMS collaboration, the can be probed at the future experiment by SuperCDMS at Stage-C.

Appendix D: Dark matter indirect detection from gamma-ray

WIMPs annihilation in the halo may lead to a flux of gamma-rays, with both continuum and line contributions. The former can be produced as continuum photons from final state radiation and the cascades of other annihilation products, whereas the latter can be emission from loop-diagrams to $\gamma\gamma$, γZ or γh final states. Observation of monochromatic gamma rays would provide a “smoking-gun” signal for the existence of WIMPs in the halo.

The produced gamma ray flux from the annihilation of dark matter particles can be expressed as

$$\frac{\Phi_\gamma}{d\Omega dE} = \sum_i \frac{dN_\gamma^i}{dE_\gamma} \langle \sigma_i v \rangle \frac{1}{4\pi m_{DM}^2} \int_{l.o.s} \rho^2 dl, \quad (D1)$$

where ρ is the dark matter density profile, $\langle \sigma_i v \rangle$ and dN_γ^i/dE_γ are, respectively, the thermally averaged annihilation cross section times the relative velocity v and the differential gamma spectrum per annihilation coming from the decay of annihilation products of final state i . The integration is taken along the line of sight.

All the halo model dependence isolated in the integral which is given in the dimensionless form [82]

$$J(\Psi, \Delta\Omega) \equiv \frac{1}{8.5 \text{ kpc}} \left(\frac{1}{0.3 \text{ GeV/cm}^3} \right)^2 \frac{1}{\Delta\Omega} \int_{\Delta\Omega} d\Omega \int_{l.o.s} \rho^2 dl,$$

where Ψ is the angle away from the direction of the galactic center that is observed while $\Delta\Omega$ the solid angle of the field of view centered on $\Psi = 0$. After averaging $J(\Psi, \Delta\Omega)$ over a spherical solid angle $\Delta\Omega$, one obtains the photon flux as [82]

$$\frac{d\Phi}{dE_\gamma} = (5.5 \times 10^{-10} \text{ s}^{-1} \text{ cm}^{-2}) \frac{dN_\gamma^i}{dE_\gamma} \left(\frac{\langle \sigma_i v \rangle}{\text{pb}} \right) \left(\frac{100 \text{ GeV}}{m} \right)^2 \bar{J}(\Psi, \Delta\Omega) \Delta\Omega, \quad (D2)$$

where the function \bar{J} contains all information about the dark matter distribution in the halo. The above equation can be factorized into two parts: $\bar{J}(\Psi, \Delta\Omega) \Delta\Omega$ (astrophysics) and other terms describing the dark matter annihilation and the fragmentation of its annihilation products (particle physics). The latter can be determined from microscopic measurement, but the former exhibits considerable uncertainties involved in the distribution of dark matter in the Galactic center region. For example, at $\Delta\Omega = 10^{-3} \text{ sr}$, characteristic of ground-based Atmospheric Cerenkov Telescopes (ACTs), typical values of \bar{J} range from 10^3 for the NFW profile [65, 66], to about 10^5 for the profile of Moore, *et al.* [83]. Furthermore, as the distribution of dark matter might be clumpy, this inhomogeneity effect would enhance indirect detection rates by a “boost factor”, defined as

$$B \equiv \frac{\langle \rho^2 \rangle}{\langle \rho \rangle^2}. \quad (D3)$$

If the dark matter were locally distributed completely evenly, the boost factor would be equal to one. Small-scale structure of dark matter, however, enhance this quantity to a large value.

The particle physics model dependence enters through all the other factor in Eq. D1. The energy integral is roughly $\int dE dN_\gamma^i/dE \sim 0.5$ for all i , but the energy distribution depends significantly on the annihilation channel. Note that the resulting photon spectra depend only on the initial energies of the annihilation products and not on the details of the WIMPs annihilation process. The spectra have been studied using PYTHIA [84], and a simple analytic fit has been presented in Refs. [82, 85] for the most important annihilation channels as follows:

$$\frac{dN_\gamma}{dx} = \frac{a}{x^{1.5}} e^{-bx},$$

where $x \equiv E_\gamma/m_{DM}$ and $(a, b) = (0.73, 7.76)$ for WW and ZZ , $(1.0, 10.7)$ for $b\bar{b}$, $(1.1, 15.1)$ for $t\bar{t}$, and $(0.95, 6.5)$ for $u\bar{u}$. In most cases the spectrum produced does not vary much. The only exception to this is the somewhat harder spectrum generated through annihilation to $\tau^+\tau^-$. Particle physics models, however, very rarely predict a dark matter candidate that annihilates mostly to $\tau^+\tau^-$. In this work we focus our attention only on the annihilation channel involving the heavy fermion, gauge boson and Higgs boson.

The integrated photon flux above some photon energy threshold E_{th} is [85]

$$\begin{aligned} \Phi_\gamma(E_{th}) = & \left(5.5 \times 10^{-10} \text{s}^{-1} \text{cm}^{-2}\right) \left(\frac{100 \text{ GeV}}{m}\right)^2 \bar{J}(\Psi, \Delta\Omega) \Delta\Omega \\ & \times \sum_i \left(\frac{\langle\sigma_i v\rangle}{\text{pb}}\right) \int_{E_{th}}^{m_D} dE_\gamma \frac{dN_\gamma^i}{dE_\gamma}, \end{aligned} \quad (\text{D4})$$

where the sum is over all possible annihilation channels. Detectors also have upper cutoffs, but these are typically irrelevant, as the energy distribution falls steeply with energy. In this work we consider two representative E_{th} : 1 GeV, accessible to space-based detectors, and 50 GeV, characteristic of ground-based telescopes.

-
- [1] A. W. Strong *et al.*, *Astron. Astrophys.* **444**, 495 (2005), astro-ph/0509290.
 - [2] J. Chang *et al.*, *Nature* **456**, 362 (2008).
 - [3] PAMELA, O. Adriani *et al.*, *Nature* **458**, 607 (2009), arXiv:0810.4995.
 - [4] The Fermi LAT, A. A. Abdo *et al.*, *Phys. Rev. Lett.* **102**, 181101 (2009), arXiv:0905.0025.
 - [5] Z. Ahmed *et al.* [The CDMS-II Collaboration], *Science* **327**, 1619 (2010), arXiv:0912.3592.
 - [6] M. Kadastik, K. Kannike, A. Racioppi and M. Raidal, *Phys. Rev. Lett.* **104**, 201301 (2010), arXiv:0912.2729.

- [7] M. Kadastik, K. Kannike, A. Racioppi and M. Raidal, Phys. Lett. B **694**, 242 (2010), arXiv:0912.3797.
- [8] A. Bottino, F. Donato, N. Fornengo and S. Scopel, Phys. Rev. D **81**, 107302 (2010), arXiv:0912.4025.
- [9] D. Feldman, Z. Liu and P. Nath, Phys. Rev. D **81**, 095009 (2010), arXiv:0912.4217.
- [10] M. Ibe and T. T. Yanagida, Phys. Rev. D **81**, 035017 (2010), arXiv:0912.4221.
- [11] J. Kopp, T. Schwetz and J. Zupan, JCAP **1002**, 014 (2010), arXiv:0912.4264.
- [12] R. Allahverdi, B. Dutta and Y. Santoso, Phys. Lett. B **687**, 225 (2010), arXiv:0912.4329.
- [13] M. Endo, S. Shirai and K. Yonekura, JHEP **1003**, 052 (2010), arXiv:0912.4484.
- [14] Q. H. Cao, I. Low and G. Shaughnessy, Phys. Lett. B **691**, 73 (2010), arXiv:0912.4510.
- [15] M. Holmes and B. D. Nelson, Phys. Rev. D **81**, 055002 (2010), arXiv:0912.4507.
- [16] G. Jungman, M. Kamionkowski, and K. Griest, Phys. Rept. **267**, 195 (1996), hep-ph/9506380.
- [17] G. Bertone, D. Hooper, and J. Silk, Phys. Rept. **405**, 279 (2005), hep-ph/0404175.
- [18] G. Servant and T. M. P. Tait, Nucl. Phys. **B650**, 391 (2003), hep-ph/0206071.
- [19] H.-C. Cheng, J. L. Feng, and K. T. Matchev, Phys. Rev. Lett. **89**, 211301 (2002), hep-ph/0207125.
- [20] G. Servant and T. M. P. Tait, New J. Phys. **4**, 99 (2002), hep-ph/0209262.
- [21] H.-C. Cheng and I. Low, JHEP **09**, 051 (2003), hep-ph/0308199.
- [22] H.-C. Cheng and I. Low, JHEP **08**, 061 (2004), hep-ph/0405243.
- [23] A. Birkedal, A. Noble, M. Perelstein, and A. Spray, Phys. Rev. **D74**, 035002 (2006), hep-ph/0603077.
- [24] V. Silveira and A. Zee, Phys. Lett. **B161**, 136 (1985).
- [25] J. McDonald, Phys. Rev. **D50**, 3637 (1994), hep-ph/0702143.
- [26] V. Barger, P. Langacker, H.-S. Lee, and G. Shaughnessy, Phys. Rev. **D73**, 115010 (2006), hep-ph/0603247.
- [27] R. Barbieri, L. J. Hall, and V. S. Rychkov, Phys. Rev. **D74**, 015007 (2006), hep-ph/0603188.
- [28] L. Lopez Honorez, E. Nezri, J. F. Oliver, and M. H. G. Tytgat, JCAP **0702**, 028 (2007), hep-ph/0612275.
- [29] M. Gustafsson, E. Lundstrom, L. Bergstrom, and J. Edsjo, Phys. Rev. Lett. **99**, 041301 (2007), astro-ph/0703512.
- [30] V. Barger, P. Langacker, M. McCaskey, M. J. Ramsey-Musolf, and G. Shaughnessy, Phys.

- Rev. **D77**, 035005 (2008), arXiv:0706.4311.
- [31] Q.-H. Cao, E. Ma, and G. Rajasekaran, Phys. Rev. **D76**, 095011 (2007), arXiv:0708.2939.
 - [32] Q.-H. Cao, E. Ma, and G. Shaughnessy, Phys. Lett. **B673**, 152 (2009), arXiv:0901.1334.
 - [33] M. Kadastik, K. Kannike and M. Raidal, Phys. Rev. D **81**, 015002 (2010), arXiv:0903.2475,
 - [34] M. Kadastik, K. Kannike, and M. Raidal, Phys. Rev. **D80**, 085020 (2009), arXiv:0907.1894.
 - [35] H. Zhang, C. S. Li, Q. H. Cao and Z. Li, Phys. Rev. D **82**, 075003 (2010), arXiv:0910.2831.
 - [36] F. Wilczek, Int. J. Mod. Phys. A **23**, 1791 (2008), [Eur. Phys. J. C **59**, 185 (2009)], arXiv:0708.4236.
 - [37] V. Barger, W.-Y. Keung, and G. Shaughnessy, Phys. Rev. **D78**, 056007 (2008), arXiv:0806.1962.
 - [38] M. Beltran, D. Hooper, E. W. Kolb, and Z. C. Krusberg, Phys. Rev. **D80**, 043509 (2009), arXiv:0808.3384.
 - [39] W. Shepherd, T. M. P. Tait, and G. Zaharijas, Phys. Rev. **D79**, 055022 (2009), arXiv:0901.2125.
 - [40] J. Goodman, M. Ibe, A. Rajaraman, W. Shepherd, T. M. P. Tait and H. B. Yu, Phys. Rev. D **82**, 116010 (2010), arXiv:1008.1783.
 - [41] J. Goodman, M. Ibe, A. Rajaraman, W. Shepherd, T. M. P. Tait and H. B. Yu, Nucl. Phys. B **844**, 55 (2011), arXiv:1009.0008.
 - [42] J. Goodman, M. Ibe, A. Rajaraman, W. Shepherd, T. M. P. Tait and H. B. Yu, Phys. Lett. B **695**, 185 (2011), arXiv:1005.1286;
 - [43] P. Agrawal, Z. Chacko, C. Kilic and R. K. Mishra, arXiv:1003.5905 [hep-ph].
 - [44] P. Agrawal, Z. Chacko, C. Kilic and R. K. Mishra, arXiv:1003.1912.
 - [45] Y. Bai, P. J. Fox and R. Harnik, JHEP **1012**, 048 (2010), arXiv:1005.3797.
 - [46] J. Fan, M. Reece and L. T. Wang, JCAP **1011**, 042 (2010), arXiv:1008.1591.
 - [47] W. Buchmuller and D. Wyler, Nucl. Phys. **B268**, 621 (1986).
 - [48] C. Arzt, M. B. Einhorn, and J. Wudka, Nucl. Phys. **B433**, 41 (1995), hep-ph/9405214.
 - [49] Particle Data Group, C. Amsler *et al.*, Phys. Lett. **B667**, 1 (2008).
 - [50] L. M. Krauss and F. Wilczek, Phys. Rev. Lett. **62**, 1221 (1989).
 - [51] P. F. Smith and J. R. J. Bennett, Nucl. Phys. **B149**, 525 (1979).
 - [52] P. F. Smith *et al.*, Nucl. Phys. **B206**, 333 (1982).
 - [53] P. Verkerk *et al.*, Phys. Rev. Lett. **68**, 1116 (1992).

- [54] E. Kolb and M. Turner, *The Early Universe (Frontiers in Physics)* (Westview Press, 1994).
- [55] WMAP, D. N. Spergel *et al.*, *Astrophys. J. Suppl.* **170**, 377 (2007), astro-ph/0603449.
- [56] B. C. Allanach, G. Belanger, F. Boudjema, and A. Pukhov, *JHEP* **12**, 020 (2004), hep-ph/0410091.
- [57] M. M. Nojiri, G. Polesello, and D. R. Tovey, *JHEP* **03**, 063 (2006), hep-ph/0512204.
- [58] E. A. Baltz, M. Battaglia, M. E. Peskin, and T. Wizansky, *Phys. Rev.* **D74**, 103521 (2006), hep-ph/0602187.
- [59] Y. G. Kim and K. Y. Lee, *Phys. Rev.* **D75**, 115012 (2007), hep-ph/0611069.
- [60] Q.-H. Cao, E. Ma, J. Wudka, and C. P. Yuan, arXiv:0711.3881.
- [61] J. Angle *et al.* [XENON Collaboration], *Phys. Rev. Lett.* **100**, 021303 (2008), arXiv:0706.0039.
- [62] CDMS, D. S. Akerib *et al.*, *Phys. Rev. Lett.* **96**, 011302 (2006), astro-ph/0509259.
- [63] D. S. Akerib *et al.*, *Nucl. Instrum. Meth.* **A559**, 411 (2006).
- [64] GLAST, A. Morselli, A. Lionetto, A. Cesarini, F. Fucito, and P. Ullio, *Nucl. Phys. Proc. Suppl.* **113**, 213 (2002), astro-ph/0211327.
- [65] J. F. Navarro, C. S. Frenk, and S. D. M. White, *Astrophys. J.* **462**, 563 (1996), astro-ph/9508025.
- [66] J. F. Navarro, C. S. Frenk, and S. D. M. White, *Astrophys. J.* **490**, 493 (1997), astro-ph/9611107.
- [67] G. Johannesson, talk at the XLIVth Rencontres de Moriond, La Thuile, February 18, 2009. <http://moriond.in2p3.fr/J09/transparentes/johannesson.pdf>.
- [68] L. Reyes, talk at SnowPAC 2009: Snowbird Workshop on Particle Astrophysics, Astronomy and Cosmology, February 19, 2009.
- [69] V. Barger, Y. Gao, W. Y. Keung, D. Marfatia and G. Shaughnessy, *Phys. Lett. B* **678**, 283 (2009), arXiv:0904.2001.
- [70] H. F. W. Sadrozinski, *Nucl. Instrum. Meth.* **A466**, 292 (2001).
- [71] the MAGIC Telescope, D. Petry, *Astron. Astrophys. Suppl. Ser* **138**, 601 (1999), astro-ph/9904178.
- [72] C. Baixeras *et al.*, astro-ph/0403180.
- [73] M. E. Peskin, *J. Phys. Soc. Jap.* **76**, 111017 (2007), arXiv:0707.1536.
- [74] V. M. Abazov *et al.* [D0 Collaboration], *Phys. Rev. Lett.* **90**, 251802 (2003), hep-ex/0302014.
- [75] T. Aaltonen *et al.* [CDF Collaboration], *Phys. Rev. Lett.* **101**, 181602 (2008), arXiv:0807.3132.

- [76] G. Bertone, C. B. Jackson, G. Shaughnessy, T. M. P. Tait, and A. Vallinotto, Phys. Rev. **D80**, 023512 (2009), arXiv:0904.1442.
- [77] C. B. Jackson, G. Servant, G. Shaughnessy, T. M. P. Tait and M. Taoso, JCAP **1004**, 004 (2010), arXiv:0912.0004.
- [78] G. K. Mallot, hep-ex/9912040.
- [79] A. Bottino, F. Donato, N. Fornengo, and S. Scopel, Astropart. Phys. **18**, 205 (2002), hep-ph/0111229.
- [80] J. R. Ellis, K. A. Olive, Y. Santoso, and V. C. Spanos, Phys. Rev. **D71**, 095007 (2005), hep-ph/0502001.
- [81] Particle Data Group, W. M. Yao *et al.*, J. Phys. **G33**, 1 (2006).
- [82] L. Bergstrom, P. Ullio, and J. H. Buckley, Astropart. Phys. **9**, 137 (1998), astro-ph/9712318.
- [83] B. Moore *et al.*, Astrophys. J. **524**, L19 (1999).
- [84] T. Sjostrand, S. Mrenna, and P. Z. Skands, JHEP **05**, 026 (2006), hep-ph/0603175.
- [85] J. L. Feng, K. T. Matchev, and F. Wilczek, Phys. Rev. **D63**, 045024 (2001), astro-ph/0008115.